



## OPEN ACCESS

## EDITED BY

Robin Campion,  
National Autonomous University of  
Mexico, Mexico

## REVIEWED BY

Wolfgang Stremme,  
National Autonomous University of  
Mexico, Mexico  
Simon Carn,  
Michigan Technological University,  
United States  
Pasquale Sellitto,  
UMR7583 Laboratoire inter-  
universitaire des systèmes  
atmosphériques (LISA), France

## \*CORRESPONDENCE

Jean-François Smekens,  
✉ Francois.Smekens@earth.ox.ac.uk

## SPECIALTY SECTION

This article was submitted to  
Volcanology,  
a section of the journal  
Frontiers in Earth Science

RECEIVED 28 July 2022

ACCEPTED 13 December 2022

PUBLISHED 06 January 2023

## CITATION

Smekens J-F, Mather TA, Burton MR,  
La Spina A, Kabbabe K, Esse B, Varnam M  
and Grainger RG (2023), Quantification  
of gas, ash, and sulphate aerosols in  
volcanic plumes from open path Fourier  
transform infrared (OP-FTIR) emission  
measurements at Stromboli  
volcano, Italy.  
*Front. Earth Sci.* 10:1005738.  
doi: 10.3389/feart.2022.1005738

## COPYRIGHT

© 2023 Smekens, Mather, Burton, La  
Spina, Kabbabe, Esse, Varnam and  
Grainger. This is an open-access article  
distributed under the terms of the  
[Creative Commons Attribution License  
\(CC BY\)](https://creativecommons.org/licenses/by/4.0/). The use, distribution or  
reproduction in other forums is  
permitted, provided the original  
author(s) and the copyright owner(s) are  
credited and that the original  
publication in this journal is cited, in  
accordance with accepted academic  
practice. No use, distribution or  
reproduction is permitted which does  
not comply with these terms.

# Quantification of gas, ash, and sulphate aerosols in volcanic plumes from open path Fourier transform infrared (OP-FTIR) emission measurements at Stromboli volcano, Italy

Jean-François Smekens<sup>1\*</sup>, Tamsin A. Mather<sup>1</sup>, Mike R. Burton<sup>2</sup>,  
Alessandro La Spina<sup>3</sup>, Khristopher Kabbabe<sup>4</sup>, Benjamin Esse<sup>2</sup>,  
Matthew Varnam<sup>2,5</sup> and Roy G. Grainger<sup>6</sup>

<sup>1</sup>Department of Earth Sciences, University of Oxford, Oxford, United Kingdom, <sup>2</sup>Department of Earth and Environmental Sciences, University of Manchester, Manchester, United Kingdom, <sup>3</sup>Istituto Nazionale di Geofisica e Vulcanologia, Osservatorio Etneo, Catania, Italy, <sup>4</sup>Department of Mechanical, Aerospace and Civil Engineering, University of Manchester, Manchester, United Kingdom, <sup>5</sup>Lunar and Planetary Laboratories, University of Arizona, Tucson, AZ, United States, <sup>6</sup>COMET, Atmospheric, Oceanic and Planetary Physics, University of Oxford, Oxford, United Kingdom

Field-portable Open Path Fourier Transform Infrared (OP-FTIR) spectrometers can be used to remotely measure the composition of volcanic plumes using absorption spectroscopy, providing invaluable data on total gas emissions. Quantifying the temporal evolution of gas compositions during an eruption helps develop models of volcanic processes and aids in eruption forecasting. Absorption measurements require a viewing geometry which aligns infrared source, plume, and instrument, which can be challenging. Here, we present a fast retrieval algorithm to estimate quantities of gas, ash and sulphate aerosols from thermal emission OP-FTIR measurements, and the results from two pilot campaigns on Stromboli volcano in Italy in 2019 and 2021. We validate the method by comparing time series of SO<sub>2</sub> slant column densities retrieved using our method with those obtained from a conventional UV spectrometer, demonstrating that the two methods generally agree to within a factor of 2. The algorithm correctly identifies ash-rich plumes and gas bursts associated with explosions and quantifies the mass column densities and particle sizes of ash and sulphate aerosols (SA) in the plume. We compare the ash sizes retrieved using our method with the particle size distribution (PSD) of an ash sample collected during the period of measurements in 2019 by flying a Remotely Piloted Aircraft System into the path of a drifting ash plume and find that both modes of the bimodal PSD (a fine fraction with diameter around 5–10 μm and a coarse fraction around 65 μm) are identified within our datasets at different times. We measure a decrease in the retrieved ash particle size with distance downwind, consistent with settling of larger particles, which we also observed visually. We measure a decrease in the SO<sub>2</sub>/SA ratio as the plume travels downwind, coupled with an increase in measured SA particle size (range 2–6 μm), suggesting rapid hygroscopic particle growth and/or SO<sub>2</sub>

oxidation. We propose that infrared emission spectroscopy can be used to examine physical and chemical changes during plume transport and opens the possibility of remote night-time monitoring of volcanic plume emissions. These ground-based analyses may also aid the refinement of satellite-based aerosol retrievals.

#### KEYWORDS

OP-FTIR, volcanic gases, volcanic aerosols, plume chemistry, Stromboli, remotely piloted aircraft system, UAS

## 1 Introduction

Emissions of gas and particulate matter accompany volcanic activity of all types, from mild effusive eruptions to large explosions. They form volcanic plumes consisting of a mixture of gases and particulates, including sulphate aerosols (SA) and sometimes volcanic ash (Carey and Bursik, 2015), which interact with the atmosphere as they travel away from their source, affecting the environment locally, and sometimes regionally or globally (Delmelle, 2003; Mather, 2015). Depending on the intensity of the emissions, the duration of a particular eruptive episode and the injection height, volcanic emissions can present significant hazards to local populations (Horwell, 2007; Gudmundsson, 2011; Tang et al., 2020; Carlsen et al., 2021), infrastructures (Barsotti et al., 2010; Wilson et al., 2014) and air traffic (Carn et al., 2009; Schmidt et al., 2014). The emergence of automated, continuous monitoring of volcanic plume composition provides valuable insights into the behaviour of volatiles over the course of volcanic crises and technical advances in instrumentation now offer new possibilities to measure plume composition in real-time and in a safe manner (Kern et al., 2022). Here we present a new method to measure gas and particle composition in volcanic plumes using an Open Path Fourier Transform Infrared (OP-FTIR) spectrometer collecting passive emission measurements.

FTIR spectroscopy is a powerful tool to identify and quantify atmospheric composition, as a number of trace gases present distinctive rotational and vibrational features at wavelengths from the near-infrared to the far-infrared. Since the emergence of relatively portable OP-FTIR spectrometers, it has been used extensively by the volcanic gas community over the past 30 years (Notsu et al., 1993; Mori et al., 1995; Mori and Notsu, 1997; Oppenheimer et al., 1998a; Francis et al., 1998; Horrocks et al., 1999; Horrocks et al., 2001). The most common method utilizes hot eruptive material (lava flow, lava dome, lava fountains, etc.) as a source of infrared (IR) radiation to measure the absorption features of the emitted gases directly at the source (Burton et al., 2000; Burton et al., 2007; La Spina et al., 2015; Pfeiffer et al., 2018). In order to target passive gas plumes, measurements can also be performed by using the Sun or the Moon as the source of radiation, a method known as solar/lunar occultation (Francis et al., 1998; Burton et al., 2001; Duffell et al., 2001; Butz et al., 2017); or, when the plume travels at or passes

through, ground-level, using an artificial IR radiation source placed on the other side of the plume from the observer or combined with a mirror to achieve a longer path length (Burton et al., 2000; Vanderkluysen et al., 2014). These methods all rely on the principle of absorption spectroscopy, whereby the variable of interest (i.e., the quantity of a given gas species) is related to the strength of absorption of radiation by said gas, and the gas quantity is retrieved by fitting a modelled spectrum to the measured spectrum (Burton et al., 2000; Burton et al., 2007). While absorption spectroscopy using a hot radiation source ( $>300^{\circ}\text{C}$ ) offers the key advantage of a relatively simple retrieval of the amounts of the most abundant volcanic gases, a specific geometry to align a hot source, the volcanic plume and the instrument is required. This is quite straightforward to achieve when using the Sun as a source of radiation, but the long atmospheric path then precludes quantification of key gases such as  $\text{CO}_2$  and  $\text{H}_2\text{O}$ , although near-infrared solar retrievals of volcanic  $\text{CO}_2$  have been demonstrated (Butz et al., 2017). OP-FTIR is most useful when there is explosive volcanic activity, as this provides an ample radiation source. In the case of ash-rich eruption columns only the cooler gas on the outside of the plume is measurable, but this is sufficient to produce accurate retrievals of the key gas species. In these conditions *in-situ* sensors are extremely challenging to use, so OP-FTIR provides the best opportunity for gas quantification. This has been successfully applied to plumes from effusive or fire fountaining activity using incandescent vents and flows as a source of radiation (Allard et al., 2005; Edmonds and Gerlach, 2007; La Spina et al., 2010; La Spina et al., 2015; Allard et al., 2016), or passive emissions using artificial sources (Burton et al., 2000; Vanderkluysen et al., 2014; Sellitto et al., 2019). When using solar/lunar occultation (Burton et al., 2001; Duffell et al., 2001; Butz et al., 2017), available time windows for measurements are also constrained by the position of the celestial objects in the sky. OP-FTIR is generally used for short regular measurements, where data are collected for a few minutes, rather than for continuous monitoring. One example of continuous monitoring is the Cerberus instrument on Stromboli volcano in Italy (La Spina et al., 2013), a system using hot rocks from the crater walls as a source of IR radiation and capable of determining gas composition from individual vents, which operated between 2009 and 2019 when it was destroyed by a paroxysm episode. Long-term regular ( $\sim$ weekly) solar FTIR measurements of  $\text{SO}_2$ , HCl and HF have been conducted on

Mt Etna in Italy, and regular daytime measurements of the plume of Popocatepetl volcano in Mexico have been conducted for 4 years (Taquet et al., 2019) using a solar-tracking OP-FTIR instrument originally meant for long-term atmospheric composition monitoring, and which intersected the passive emissions generated by the nearby volcano when the wind direction was favourable.

In contrast, emission spectroscopy quantifies the radiance produced by volcanic gases when viewed against a cold background (i.e., a clear sky or clouds at higher altitudes). The method was first introduced to volcanology by Love et al. (1998), and used to quantify volcanic gases in the gas plume produced by Popocatepetl volcano in Mexico (Love et al., 1998; Love et al., 2000; Goff et al., 2001). The main assumption of the method is of a thermal contrast between a cold sky and a relatively warmer plume. It is therefore best suited for plumes measured close to their emission source (where they are more likely to be warmer than the background atmosphere) and with a relatively high viewing angle, both of which are factors maximizing the thermal contrast. Following these early efforts, the method had been largely unused until more recent studies, once again at Popocatepetl, demonstrated its use for routine measurements of a passive plume (Stremme et al., 2012; Taquet et al., 2017). These most recent efforts focus exclusively on gases, using individual, relatively narrow retrieval windows dedicated to each target gas. When using absorption spectroscopy, the strength of absorption for various gases is quantified by reproducing the observed unprocessed intensity signal (i.e., without performing radiometric calibration), with a model in which the source intensity is simulated by a polynomial function that represents a series of physical parameters, including the Planck function for the source temperature, the instrument response function and, crucially, the broadband absorption of light by particulate species. Similarly, in previous emission studies (Love et al., 1998; Love et al., 2000; Goff et al., 2001; Stremme et al., 2012; Taquet et al., 2017), particulate species which are likely often present in the volcanic plume are treated as interfering with the retrieval and require a correction during data processing or are dismissed during quality control. However, the radiometric calibration performed during the pre-processing stage of emission measurements provides a way of characterizing most of the physical parameters which form the polynomial function described above, and therefore presents a unique opportunity to isolate and quantify the contribution from species with broader spectral features, such as sulphate aerosols and ash. Sellitto et al. (2019) have shown that the simultaneous retrieval of SO<sub>2</sub> and sulphate aerosols is possible from active absorption measurements where the intensity of the radiative source can be assumed to remain constant. They show that the presence of sulphate aerosols may lead to significant overestimation in SO<sub>2</sub> amounts if not accounted for. Accurate quantification of particulate matter (PM) concentration and size

in plumes is also important in its own right when forecasting, for example, the respiratory hazards and environmental consequences associated with volcanic emissions (e.g., Ilyinskaya et al., 2017).

In this study we present a fast retrieval algorithm capable of simultaneously extracting slant column densities (SCDs) of gas and particles from OP-FTIR data collected in emission mode in near real-time, using a broad fitting window.

## 2 Methods

### 2.1 Data acquisition strategy

We present data from two separate measurement campaigns at Stromboli volcano in Italy: September 9–11, 2019, and September 23–25, 2021 (Figure 1). Thermal emission measurements were performed using a Bruker EM27 OP-FTIR spectrometer lent by the Osservatorio Etneo dell'Istituto Nazionale di Geofisica e Vulcanologia (INGV). The EM27 consists of a “Rock Solid interferometer” (corner cube mirrors on a pendulum around the beam splitter) directing radiation towards a Stirling-cooled Mercury-Cadmium-Telluride (MCT) detector using entirely reflective optics (i.e., no external telescope was added) with an optical path difference of 1.8 cm and a field-of view (FOV) of 30 mrad. Spectra were acquired in the frequency range 600–2,000 cm<sup>-1</sup> with a resolution of ~0.5 cm<sup>-1</sup> (or a ~0.25 cm<sup>-1</sup> spectral sampling), and averaged with five co-adds, resulting in a sampling interval of 8–10 s. Radiometric calibration was performed using an internal blackbody target with adjustable temperature. Using two blackbody spectra at two different temperatures (typically around 20°C and 40°C), we created an instrument calibration function which can be applied to convert the single beam spectrum to calibrated radiance or brightness temperature. Clear sky spectra were collected by pointing the instrument towards an area of sky outside of the plume while keeping the inclination angle as close to that of the plume measurements as possible. The duration of acquisition periods varied between 30 min and several hours, and calibration and clear sky measurements were performed every hour or so to account for the thermal drift of the instrument and to reflect changing atmospheric conditions. In datasets for which multiple calibration sets were acquired, we account for instrument drift by interpolating the blackbody spectra between the calibration sets, thereby creating a time-dependent calibration function with unique values for each measurement. We also create a similar time-dependent representation of the expected background spectrum by interpolating between clear sky spectra. This is especially important when working with longer datasets or with datasets acquired at the time of local sunrise and sunset, when the thermal profile of the atmosphere changes rapidly.

During the first field campaign in 2019, measurements were performed from the l'Osservatorio restaurant, providing a direct

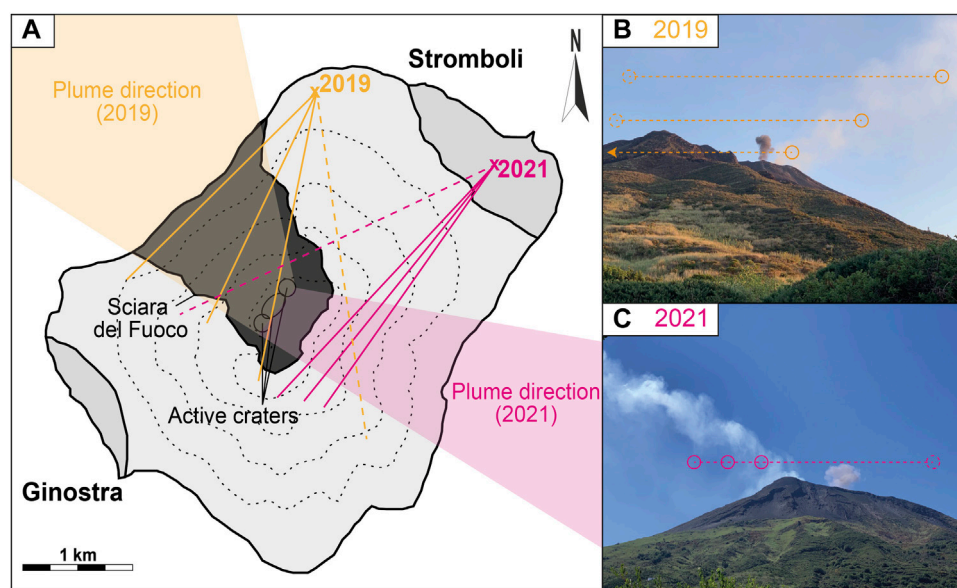


**FIGURE 1**

(A) Sketch map of the island of Stromboli, depicting the measurement locations and approximate plume geometries during the two measurement campaigns [2019 in yellow, 2021 in magenta]. Grey shaded areas (labeled Stromboli and Ginostra) represent settlements on the island. The black shaded area represents the collapse feature known as the *Sciara del Fuoco*. The approximate location of the three main crater areas (Northeast, Central and Southwest) is indicated by ellipses. Shaded coloured polygons represent the general plume direction during measurements. Coloured lines represent the range of azimuths during plume (solid) and clear sky (dashed) measurements (B and C) Photographs taken from the measurement location in the 2019 (B) and 2021 (C) campaigns. Circles represent the approximate location of the instrument field of view during plume (solid) and clear sky (dashed) measurements.

view of the craters (Figure 1). Wind direction was relatively constant during the 3-day period, and the plume drifted over the *Sciara del Fuoco* in a NE direction. We collected multiple short sets of 30–60 min of measurements, moving the instrument field-of-view to intersect the plume at various distances from the vent. The activity during this campaign was typical for Stromboli, with explosive events occurring every 5 min on average. Events at the crater were logged manually in a notebook, with the observer entering the time, nature of the event and crater of origin as far as it was possible to observe. We also organized a series of flights with a Remotely Piloted Aircraft System (RPAS) developed and built at the University of Manchester, with the aim of sampling ash from the drifting volcanic plume during the measurement period (Figure 2). The RPAS was a quadcopter carrying a Hoover-like sampling mechanism. Once the RPAS had reached the desired location within the plume, the sampling mechanism was triggered remotely, turning on a high mass-flow ducted fan to direct airflow and ash into a small vacuum cleaner bag connected to the system. We were able to collect a single sample at 17:02 local time on 11 September 2019 (analysis results in Section 3.1). The particle size distribution (PSD) of the sample collected during the RPAS flight was measured using a Retch Camsizer X2 particle size analyser at the University of Leeds. Further, the sample was mounted onto SEM stubs using clear epoxy, polished and carbon-coated for analysis with an Electron

Microprobe Analyser (EMPA) at the University of Oxford, to determine the chemical composition of individual phases.

In 2021, measurements were performed from the roof of the Pedra Residence hotel in Stromboli village. The wind direction was approximately to the East, and the line of sight of the instrument intersected the plume as it passed over the summit of the island. We collected longer datasets (3–4 h) with the specific purpose of evaluating the usefulness of the method as a monitoring tool. A GoPro camera was used to capture time-lapse imagery from the observer's vantage point, and the eruptive events were logged by reviewing the footage. Although the method allows for a continuous record of events over long periods, weaker events and those without an associated ash-rich plume were often not detectable in the footage because we did not have a direct view of the craters. Therefore, we could not assign a specific vent to any given event either. During this second campaign, we also collected simultaneous spectra with a UV spectrometer to validate the infrared  $\text{SO}_2$  retrieval. Light was collected using a collimated telescope (diameter = 25.4 mm,  $f = 100$  mm), connected to an Ocean Optics USB 2000+ spectrometer *via* an optical fibre. The spectrometer was controlled and powered by a connected laptop *via* USB cable.  $\text{SO}_2$  slant column densities were retrieved using the iFit method (Esse et al., 2020). The wavelength window for the retrieval was 310–320 nm and

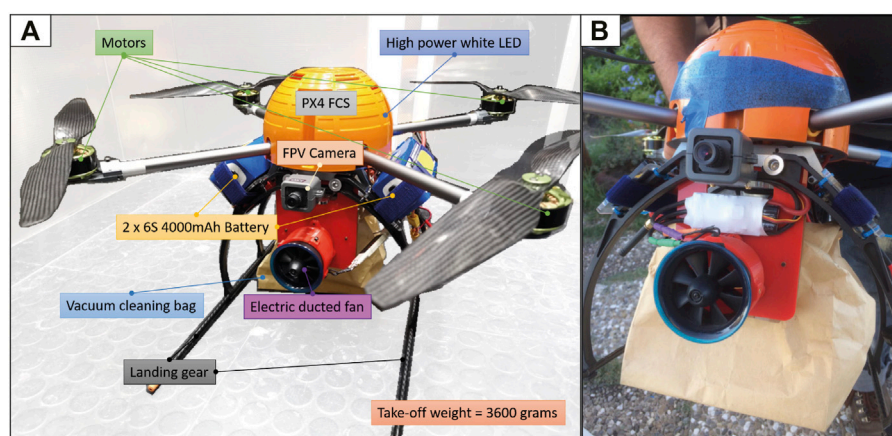


**FIGURE 2**

(A) Photograph of the Remotely Piloted Aircraft System (RPAS) used during field deployment. The red 3D printed housing seen in the middle of the multirotor houses an electric ducted fan system used to pull air and ash into the sample bag. Acronyms: LED—Light-Emitting Diode; FPV—First-Person View; FCS—Flight Controller System (B) Photograph of the RPAS after successful collection at Stromboli on 11 September 2019. Note the ash particles collected on a piece of tape affixed to the FCS housing in order to confirm plume intercept.

the fit included absorption cross-sections for  $\text{SO}_2$  at 295 K (Rufus et al., 2003) and  $\text{O}_3$  at 223 K (Serdyuchenko et al., 2014), a Ring spectrum, a wavelength shift and stretch and a linear intensity offset. The instrument line shape (ILS) was characterised using a super-Gaussian with the shape parameters also fitted for each spectrum to account for changes with time (e.g., due to changes in temperature).

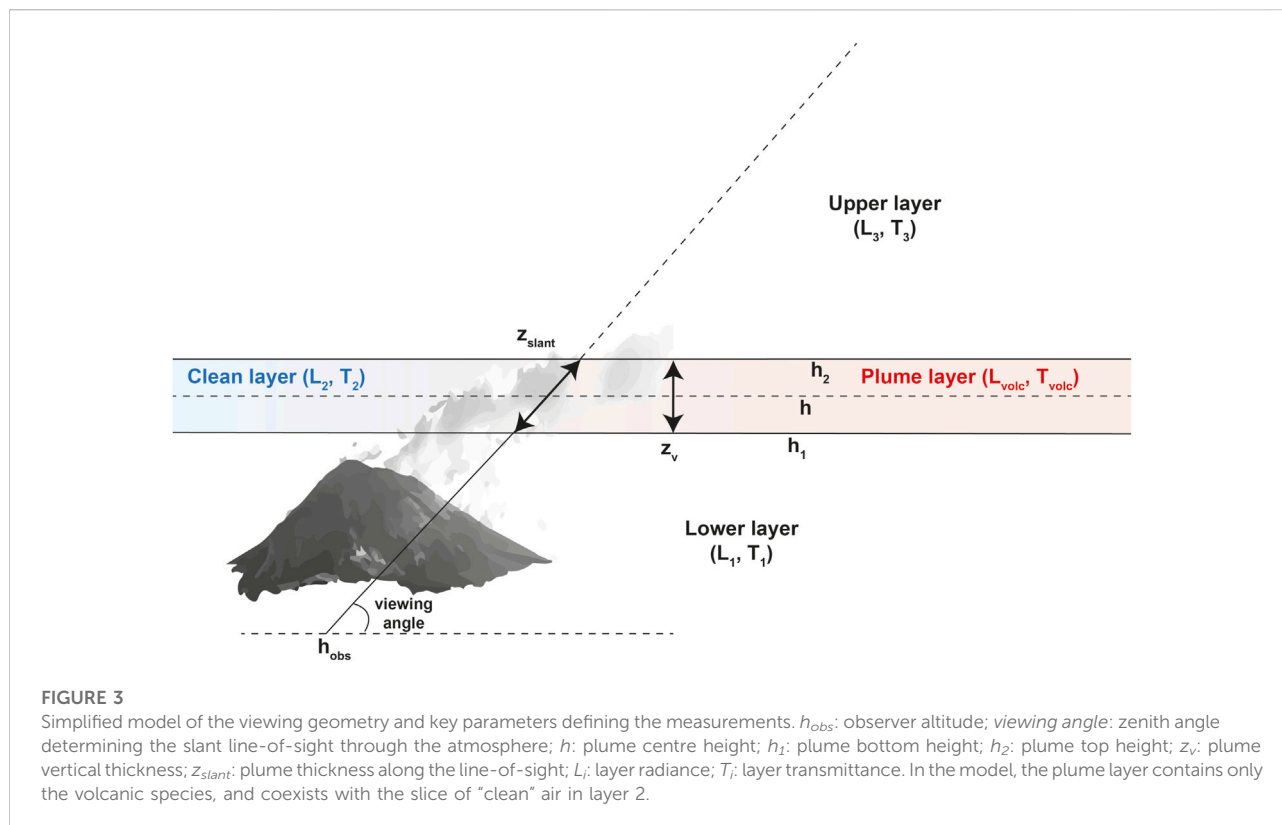
## 2.2 Retrieval algorithm

The emission spectrum retrieval algorithm (developed in Python and available at <https://www.github.com/jfsmekens/plumeIR>) follows the basic principles laid out by Love et al. (1998), where the simplified radiative transfer expression comprises three layers (Figure 3): 1) a lower layer between the observer and the plume, 2) a plume layer, and 3) an upper layer encompassing the atmosphere in the line-of-sight behind the plume. Given a plume height ( $h$ ) and a vertical plume thickness ( $z_v$ ), the plume layer is defined between the height  $h_1 = h - z_v/2$  and  $h_2 = h + z_v/2$ . The forward model computes the radiance difference between a clear sky and a plume measurement, which offers the advantage of isolating the spectral features of the volcanic species. The aim is to provide a tool which can be used in the field to quantify target species in real time as the measurements are taken (i.e., with a target processing time of <10 s for each individual spectrum, comparable to the acquisition time between consecutive spectra). The algorithm was developed around an iterative non-linear least-squares fitting method. High-resolution radiative transfer calculations ( $.04 \text{ cm}^{-1}$  spectral sampling) over the entire vertical atmospheric profile are

performed in a pre-processing stage to generate reference spectra used in the forward model. In contrast to recent efforts undertaken at Popocatepetl (Stremme et al., 2012; Taquet et al., 2017), where the effects of particulate species are simulated using a polynomial, we use a broad retrieval window ( $700\text{--}1,300 \text{ cm}^{-1}$ ) and model the radiation and attenuation due to particulate species from Mie theory, allowing us to retrieve SCDs for those species as well. The radiance difference method presents the advantage of emphasizing the spectral features due to the presence of a volcanic layer, thereby minimising the influence of atmospheric variables such as temperature and water vapour volume mixing ratios at higher altitude in the vertical profile.

### 2.2.1 Reference spectra

The first step in the retrieval is to create a set of reference radiance and optical depth spectra for each layer (Figure 4), which are then scaled in the forward model without having to perform computationally expensive radiative transfer calculations. For this task, we use the Reference Forward Model (RFM version 5), a radiative transfer model developed at the University of Oxford (Dudhia, 2017), capable of simulating atmospheric transmittance and emission at high spectral resolution using line data and reference cross-sections for individual gases extracted from the high-resolution transmission molecular absorption database (HITRAN, Rothman et al., 2009). Firstly, we determine the radiance and transmittance of each layer ( $L_x$  and  $T_x$ ) in the absence of a plume. Starting with a standard mid-latitude summer atmospheric profile evaluated with measurements from the Michelson Interferometer for Passive Atmospheric Sounding (MIPAS)



(<https://eodg.atm.ox.ac.uk/RFM/atm/>) and adjusted to reflect present-day  $\text{CO}_2$  concentration (400 ppm), we consider a small number of absorbing gases ( $\text{H}_2\text{O}$ ,  $\text{CO}_2$ ,  $\text{N}_2\text{O}$ ,  $\text{CH}_4$  and  $\text{O}_3$ ) over a broad spectral window of  $700\text{--}1,300\text{ cm}^{-1}$ . The vertical profile is then modified in the layers below 30 km to match the pressure, temperature and relative humidity from a local meteorological balloon sounding taken at a time closest to data acquisition from the station of Trapani in Sicily (launched twice daily and available at <https://weather.uwyo.edu/upperair/sounding.html>). It should be noted that Trapani is located  $>100\text{ km}$  west of Stromboli. The sounding might therefore be less representative than desired, and accuracy could be improved with dedicated local soundings. Finally, we resample the profile over an uneven vertical grid (spacing increases with altitude) with 25 layers. The profile is split into the three layers described above (Section 2.2; Figure 3) and RFM simulations are performed to extract radiance ( $L$ ), transmittance ( $T$ ), and optical depth ( $\tau$ ) for each of the three layers. Simulations are run with varying amounts of water vapour (21 steps from zero to two times the original concentrations). This allows the forward model to account for changes in relative humidity over the entire profile.

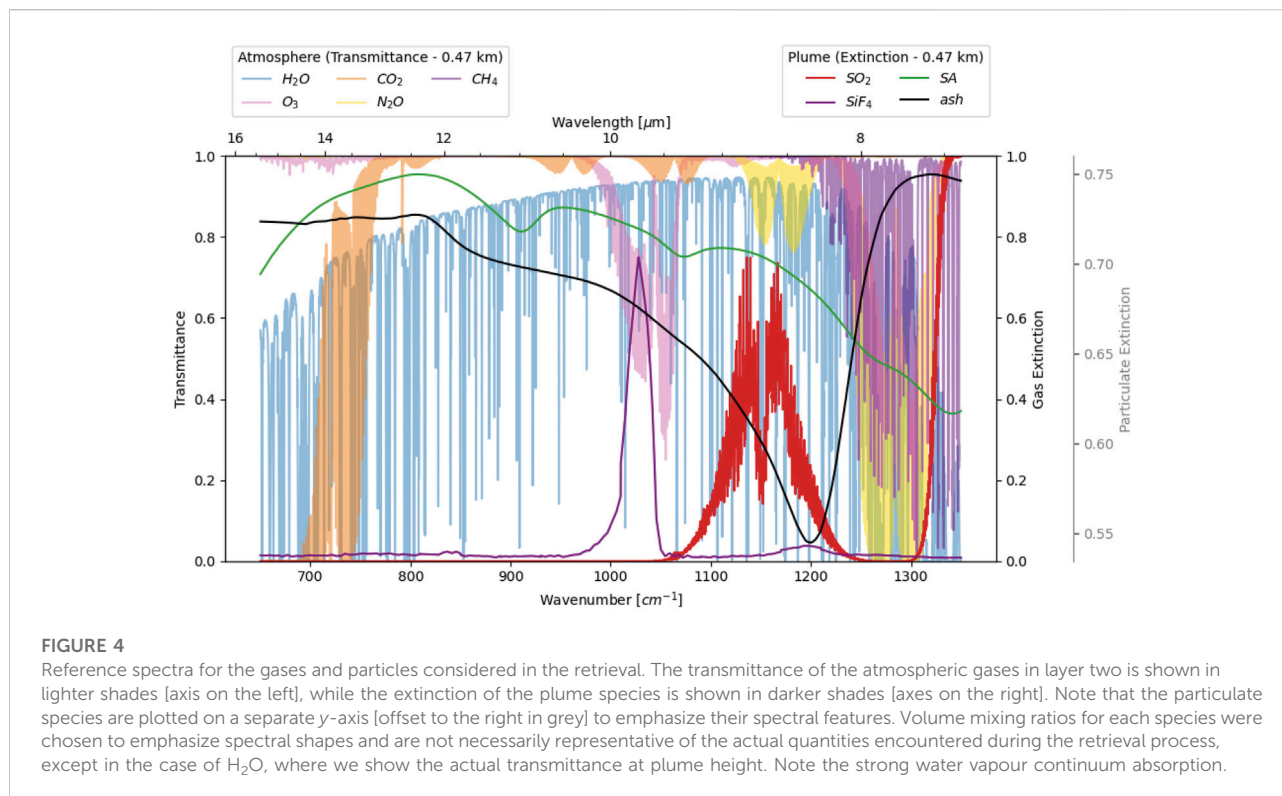
Next, we generate reference optical depth spectra for each target volcanic species ( $\text{SO}_2$ , ash and sulphate aerosols), assuming a homogeneous distribution of gas within layer 2 (Figure 4). Temperature and pressure are derived from the

atmospheric profile at the plume height, which was set at around 1 km from visual observations placing the plume just above the craters. The optical depth for each species is derived for any given volume concentration by relating it to the reference concentration as follows:

$$\tau_i = \frac{\rho_i}{\rho_{i,ref}} \tau_{i,ref} \quad (1)$$

where  $\tau_i$  is the optical depth and  $\rho_i$  is the volume mixing ratio (VMR in ppmv) for gas  $i$  within the layer. Atmospheric gases are also added as “plume” species and allowed to take positive or negative concentrations, which is meant to introduce an *ad hoc* correction in the forward model to account for small variations of the background gases in each plume measurement.

In addition to absorbing gases, we consider two types of volcanic particles: aqueous sulphate aerosols (SA) and silicate ash. For SA, we consider droplets of a binary solution of  $\text{H}_2\text{SO}_4$  and  $\text{H}_2\text{O}$ . The  $\text{H}_2\text{SO}_4$  mixing ratio and relevant temperature can be chosen by the user, and the extinction ( $\beta_{ext}$ ) and absorption ( $\beta_{abs}$ ) coefficients are calculated following Mie theory using complex refractive indices found in Lund Myhre et al. (2003) and the PyMieScatt software package (Sumlin et al., 2018). We follow a similar process for ash particles, and the user can choose between refractive indices for natural samples found in previous studies (Reed et al., 2018; Deguine et al., 2020) or calculated based on bulk chemical composition ( $\text{SiO}_2$  wt%) using the



parameterisation found in Prata et al. (2019). Assuming a reference mass volume concentration of particles ( $1 \times 10^{-3} \text{ g cm}^{-3}$  for ash,  $5 \times 10^{-3} \text{ g cm}^{-3}$  for SA), the mass is distributed into size bins so that the number fraction follows a log-normal particle size distribution (PSD) around a mean effective diameter ( $d_{\text{eff}}$ ), which can be set by the user or retrieved as a quantitative parameter. Particle shape is not considered in the model and particles are assumed to be spherical. This assumption is reasonable for SA particles but may lead to significant differences due to inhomogeneous scattering in the case of ash particles. Figure 5 shows the expected variations in shape and intensity of the optical depth spectra in the plume layer for a given mass volume concentration as a function of chemical composition and particle size. As documented previously, the H<sub>2</sub>SO<sub>4</sub> mixing ratio has a significant effect on the expected shape of spectral extinction for aqueous SA (Biermann et al., 2000; Sellitto and Legras, 2016). However, we observe rather modest variations when considering a given mass concentration and varying the H<sub>2</sub>SO<sub>4</sub> mixing ratios (Figure 5B). Variations in particle size also lead to significant changes in the spectral features of SA (Figure 5A). Consistent with previous observations, we observe an increase in maximum extinction on the order of 20%–30% when the effective diameter increases from  $.1 \mu\text{m}$  to  $1 \mu\text{m}$ . For larger particles, the volume to surface area ratio increases dramatically, and the scattering coefficient becomes dominant in the spectral shape, leading to a flattening of

the spectral features for a given mass concentration. In this study, we have chosen to fix the chemical composition of the particle species and leave particle size as a free parameter in the retrieval.

Volcanic ash can be described according to its bulk chemical composition in terms of the relative mass percentage of silica (SiO<sub>2</sub> wt%), with values ranging from 45 wt% for the more basaltic compositions (e.g., Eyjafjallajökull 2010; Sigmundsson et al., 2010) to 75% for the most silicic (e.g., Chaitén 2008; Alfano et al., 2011). In Figures 5A, D a range of attenuations are shown for ash with bulk composition ranging from 45 to 80 wt% SiO<sub>2</sub> using the parameterization developed by Prata et al. (2019), as well as those for a selection of natural samples from several recent eruptions (Reed et al., 2018). For SA, we consider a composition of 65 wt% H<sub>2</sub>SO<sub>4</sub> - a value similar to the one recently measured by absorption FTIR spectroscopy for primary aerosols in the Masaya plume (Sellitto et al., 2019)—and use refractive indices measured for this composition by Lund Myhre et al. (2003). Ash optical depth spectra from natural samples follow a general trend with a shift of the spectral minimum and a deepening of the Si-O bond spectral feature as bulk SiO<sub>2</sub> content increases. This dependency of the position and depth of the Si-O bond absorption feature on bulk SiO<sub>2</sub> composition has been thoroughly documented within the planetary science literature (Lyon, 1965; Ramsey and Christensen, 1998; Michalski, 2004; Rogers and Nekvasil, 2015; Henderson et al., 2021), as well as within datasets using natural ash samples from recent eruptions

**TABLE 1 Retrieved parameters for the forward model along with their bounds and a priori guess.**

Symbol	Units	Parameter	A priori		Bounds
<b>Gas and particulates parameters</b>					
$\rho_{\text{gas}}$	ppmv	Gas volume mixing ratio (VMR) [CO <sub>2</sub> , O <sub>3</sub> , N <sub>2</sub> O, CH <sub>4</sub> , SO <sub>2</sub> ]	CO <sub>2</sub>	400	[1x10 <sup>-12</sup> –∞]
			O <sub>3</sub>	0.01	
			N <sub>2</sub> O	0.001	
			CH <sub>4</sub>	1.7	
			SO <sub>2</sub>	0.5	
$\rho_{\text{part}}$	g·cm <sup>-3</sup>	Particulate mass volume concentration [ash, SA]	ash	0.001	[1x10 <sup>-12</sup> –∞]
			SA	0.0005	
$d_{\text{eff}}(\text{part})$	μm	Particle effective diameter [ash, SA]	ash	2.0	[1–100]
			SA	0.5	[0.1–10]
<b>Atmospheric layers parameters</b>					
$\Delta t_{\text{prox}}$	K	Temperature difference in layer 1	0		[0–50]
$\Delta t_{\text{plume}}$	K	Temperature difference in layer 2	0		[0–50]
$\alpha_{\text{H}_2\text{O}}$	n/a	H <sub>2</sub> O scaling factor	1		[0–2]
<b>Spectral parameters</b>					
$\tilde{\nu}_{\text{shift}}$	cm <sup>-1</sup>	Frequency shift	0		[-5–5]
FOV	rad	Field of view	0.030		[0.001–0.5]

(e.g., Reed et al., 2018; Deguine et al., 2020; Piontek et al., 2021), and is accurately captured by the Prata et al. (2019) parameterization (grey shades in Figure 5D). We use a value of 51 wt% SiO<sub>2</sub> (based on the bulk composition of our sample, see Section 3.1) to calculate the reference extinction spectra for ash. A dependency of the spectral shape on particle size like that observed for SA also exists for ash.

Rather than modelling the measured radiance of a plume spectrum, the forward model replicates the radiance difference at the observer height between a plume measurement and a clear sky measurement ( $\Delta L$ ) from the parameters listed in Table 1. This is done to minimize the effects of the total atmospheric column amounts of background gases and instrument calibration and emphasize the spectral signatures of the volcanic components. The SCDs of all gas and particulate species within the plume layer are retrieved (ash, SA and SO<sub>2</sub>), along with ad hoc correction factors for O<sub>3</sub>, CO<sub>2</sub>, N<sub>2</sub>O and CH<sub>4</sub> and a scaling factor for H<sub>2</sub>O in all three layers. The size of each particulate species can also be retrieved.

Following radiative transfer theory, the radiance measured at the observer position ( $L_{\text{obs}}$ ) in this simplified model can be expressed as:

$$L_{\text{obs}} = L_1 + T_1 (L_2 + T_2 L_3) \quad (2)$$

where  $L_x$  represents the radiance and  $T_x$  the transmittance of layer  $x$ . In the presence of a volcanic plume, the slice of “clean” air in layer 2 (see Figure 3) is replaced by a plume layer, which contains the volcanic components in addition to the atmospheric gases; such that the radiance difference between a plume measurement and a clear sky measurement ( $\Delta L$ ) is:

$$\Delta L = T_1 (L_{\text{plume}} - L_2 + L_3 (T_{\text{plume}} - T_2)) \quad (3)$$

In the forward model, both the volcanic layer and the clean air slice are assigned separate optical depths. Firstly, we calculate the optical depth of the clean air slice ( $\tau_2$ ), adjusted for relative changes in water vapour content. The simple linear relationship expressed in Eq. 1) does not hold for H<sub>2</sub>O, due to the existence of a continuum absorption, such that an accurate optical depth spectrum cannot simply be scaled from a reference quantity. Instead, we calculate a series of reference spectra for a range of scaling factors (0–2) applied to the original H<sub>2</sub>O VMR at plume height. At each wavenumber  $\tilde{\nu}$ , we fit a polynomial to represent the dependency of the optical depth to the adjusted VMR, such that:

$$\tau_{2,\alpha,\tilde{\nu}} = \sum_{j=0}^p c_{j,\tilde{\nu}} \alpha^j \quad (4)$$

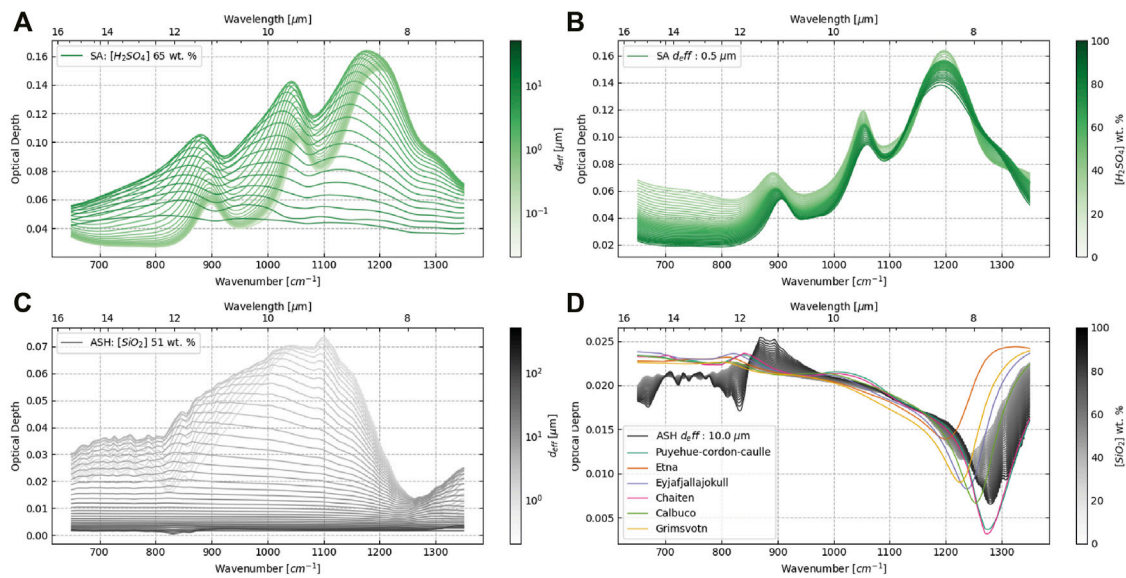


**FIGURE 5**

Optical depth reference spectra for both particle types considered in the retrieval: sulphate aerosols (SA) ((A,B)—green) and ash ((C, D)—grey) (A and C) Optical depth cross sections as a function of particle size. All reference spectra are calculated for the same mass volume concentration of  $1 \times 10^{-3} \text{ g m}^{-3}$ , and only the particle size distribution (PSD) varies. PSDs are log-normal with a mean effective diameter varying according to the colour scale (0.1–10  $\mu\text{m}$  for SA and 0.1–200  $\mu\text{m}$  for ash) and a sigma value of 1.5 (B and D) Optical depth spectra as a function of chemical composition. The effective particle diameter is kept constant (0.5  $\mu\text{m}$  for SA, 10  $\mu\text{m}$  for ash), and only the composition varies. SA compositions range from 38 to 81 wt%  $\text{H}_2\text{SO}_4$ , and spectra are calculated using refractive indices from (Lund Myhre et al., 2003). Ash bulk compositions range from 45 to 80 wt%  $\text{SiO}_2$ , and spectra are calculated using the parameterization algorithm for complex refractive indices found in (Prata et al., 2019). The mass volume concentration is again fixed at  $1 \times 10^{-3} \text{ g m}^{-3}$ . Also shown are some example spectra calculated for natural samples from recent eruptions with refractive indices found in (Deguine et al., 2020) for the same particle size.

where  $\alpha$  is the  $\text{H}_2\text{O}$  scaling factor,  $p$  is the degree of the polynomial, and  $c_j$  is the coefficient in the polynomial expression for the term of degree  $j$ . In the forward model, this set of polynomials can be used to accurately calculate optical depth spectra for any continuous value of parameter  $\alpha$  as long it is strictly restricted to within the range used in the reference set. This approach avoids having to call RFM to derive  $\text{H}_2\text{O}$  extinction coefficients during the iterative process. We found that this method is computationally much faster than a classical interpolation method and yields accurate results within the bounds of the parameterization. The adjusted transmittance for layer 2 is then simply:

$$T_{2,adj} = e^{-\tau_{2,adj}} \quad (5)$$

Next, we calculate the optical depth of the volcanic species ( $\tau_{volc}$ ) by summing individual optical depth spectra for each volcanic species:

$$\tau_{volc} = \sum_i \tau_i \quad (6)$$

where  $\tau_i$  is the optical depth for gas  $i$  derived from reference spectra calculated at the plume height and temperature using the relationship in Eq. 1). For ash and SA, we use the same

polynomial fitting approach expressed in Equation 4 to quantify the relationship between effective particle diameter and optical depth for each wavenumber (see Figure 5):

$$\tau_{i,d_{eff},\bar{v}} = \sum_{j=0}^n c_{j,\bar{v}} d_{eff}^j \quad (7)$$

where  $d_{eff}$  is the mean effective diameter of the particles for particulate species  $i$  (either ash or SA). This allows the model to accurately calculate optical depth spectra for any continuous value of  $d_{eff}$  within the bounds used in the reference set (0.1–10  $\mu\text{m}$  for SA; 1–200  $\mu\text{m}$  for ash). The transmittance of the volcanic layer ( $T_{volc}$ ) is then given simply by:

$$T_{volc} = e^{-\tau_{volc}} \quad (8)$$

The volcanic and clean layers are treated separately (i.e., each given a separate optical depth) but are geometrically occupying the same location. They have identical height, thickness and pressure, but the temperature of the plume species is allowed to differ from that of the ambient gases by a fixed amount ( $\Delta t_{plume}$ ). The radiance for each layer is calculated using the transmittances obtained in equations Eqs. 5, 6, such that the total plume radiance ( $L_{plume}$ ) is:

$$L_{plume} = B_{t_2}(1 - T_{2,adj}) + B_{(t_2+\Delta t_{plume})}(1 - T_{plume}) \quad (9)$$

where  $B_t$  is the blackbody radiance calculated using the Planck relationship,  $t_2$  is the atmospheric temperature at plume height, and  $\Delta t_{plume}$  is the temperature difference between plume and ambient temperature. This temperature difference only affects the radiance of the volcanic components and is usually set to a fixed value in our retrievals. The transmittance of the plume layer ( $T_{plume}$ ) is simply the product of the transmittance of both layers:

$$T_{plume} = T_{volc} T_{2,adj} \quad (10)$$

Each atmospheric gas is also included as an individual species in the volcanic layer in order to enable *ad hoc* corrections to compensate for small differences in total column that could arise between a clear sky measurement and the plume measurement (due to changes in temperature profiles and/or viewing angles). The VMRs and temperature of those gases is fixed within layers 1 and 3 (foreground and background) in the forward model. Adding them as free parameters within the plume layer offers a way of improving the fits around their spectral features. Large variations of the total column of H<sub>2</sub>O should also be expected, even over relatively short time windows. These can arise from changes in relative humidity and temperature over the course of the acquisition period. In contrast with previous studies where these large variations are circumvented by using spectral micro-windows in between water vapour absorption lines (e.g., Clarisse et al., 2012; Carboni et al., 2016; Sellitto and Legras, 2016; Sellitto et al., 2019; Guermazi et al., 2021), here we accounted for them using an *ad hoc* scaling factor for H<sub>2</sub>O applied to all layers. Finally, the temperature in the proximal layer (layer 1) can be modified, allowing for small changes in temperature in the proximal layer over the course of a measurement set, which results in a non-uniform offset in the measured radiance difference  $\Delta L$ . It should be noted that the mathematical expression of the forward model described above does not consider radiance scattered within the line of sight from other directions or multiple scattering.

Up to this point, all computations are performed using high-resolution RFM reference spectra. The last steps in the forward model are to 1) apply a spectral shift to the model grid (the magnitude of the frequency shift is a retrieved parameter); 2) convolve the spectrum with the ILS function (the width of the FOV is also a retrieved parameter, though the retrieved value is stable at 30 mrad throughout all our measurements); and 3) resample the convolved spectrum to match instrument resolution. The resulting radiance difference is the final processed spectrum used in the fitting algorithm. Optimal parameters are determined using an iterative non-linear least-squares method, and the Root Mean Square Error (RMSE) and coefficient of determination ( $R^2$ ) are calculated for the best fit model result.

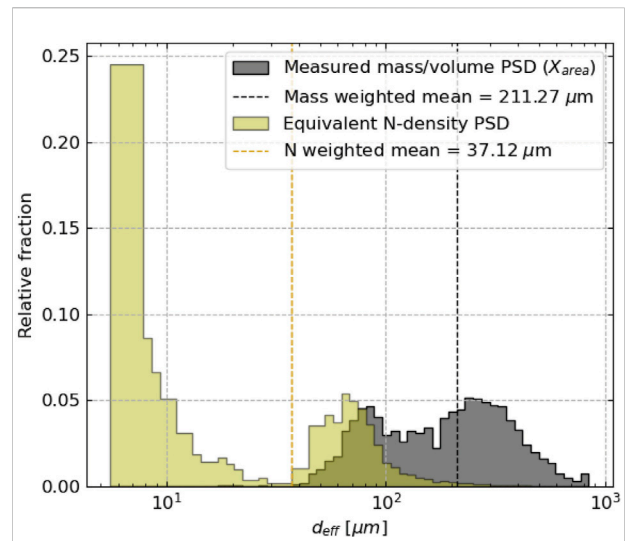


FIGURE 6

Particle size distribution (PSD) measured in the ash sample collected with the RPAS on 11 September 2019. [grey] Original measurement from Camsizer. Volumetric fraction of the particles with regards to their equivalent diameter ( $X_{area}$ : diameter of the area equivalent circle of each particle projection), yielding a mass fraction PSD with a mean at 211.17  $\mu\text{m}$ . [yellow] Number density PSD, where the relative fraction is based on the number of particles instead, converted from volumetric fraction assuming spherical particles. N-density PSD is heavily skewed towards smaller particles (mean of 37.12  $\mu\text{m}$ ) and is more directly comparable with retrieved sizes in this work.

## 3 Results

### 3.1 RPAS ash sample analysis

The ash sample collected during the first measurement campaign in 2019 was analysed for particle size and chemical composition. This section details the results of these analyses, which were used to a) guide the selection of the most appropriate ash refractive indices in the retrieval, and b) compare particle size information between the sample and the values retrieved by the algorithm. The sample's mass-equivalent PSD (Figure 6) is bimodal, with a population of coarser particles (200–400  $\mu\text{m}$ ) and a separate population of finer particles (70–100  $\mu\text{m}$ ), seemingly lacking very fine particles. This PSD is generally similar to that of fallout samples collected at the summit of Stromboli in 2015 (Freret-Lorgeril et al., 2019). However, this representation can be misleading, as the Camsizer measurement describes the volume fraction of particles based on their equivalent diameter ( $X_{area}$ : diameter of the area equivalent circle of each particle projection). In these terms, the larger particles take an outsized representation, as the very fine fraction (<10  $\mu\text{m}$ ) represents a negligible volume within the overall sample, despite representing the vast majority of the particles. In order to emphasize this effect, we also show the

**TABLE 2** Chemical composition of crystalline phases and glass measured in the ash sample collected with the RPAS on 11 September 2019.

	Glass	Ol	Cpx	Plag	Bulk
n	23	20	13	15	
Phase %	60	5	10	25	
SiO <sub>2</sub>	52.29	37.38	50.42	50.4	50.89
TiO <sub>2</sub>	1.59	0.02	0.84	0.06	1.05
Al <sub>2</sub> O <sub>3</sub>	15.42	0.03	3.22	30.12	17.11
FeO(t)	0.2	26.68	8.34	0.8	2.49
MnO	9.99	0.51	0.22	0.0	6.04
MgO	3.37	35.1	14.15	0.12	5.22
CaO	7.37	0.37	21.23	13.91	10.04
Na <sub>2</sub> O	2.89	0.01	0.37	3.23	2.58
K <sub>2</sub> O	4.04	0.0	0.14	0.59	2.59
P <sub>2</sub> O <sub>5</sub>	1.05	0.08	0.07	0.04	0.65
Cr <sub>2</sub> O <sub>5</sub>	0.0	0.0	0.02	0.01	0.0
NiO	0.0	0.04	0.01	0.01	0.01
Total	98.22	100.22	99.03	99.29	98.66

For each phase (Ol=olivine, Cpx=clinopyroxene, Plag=plagioclase), the data presented is the mean oxide composition in units of wt%, derived from *n* analyses. The *Phase %* is the relative areal fraction occupied by the phase, estimated from backscattered SEM, images. The bulk composition is the mean of all measured phases weighted according to their relative areal fraction.

PSD in terms of fractional number density (N-density) of particles by size—calculated based on the measured volume fraction and assuming spherical particles - which is heavily shifted towards smaller particle size bins. The resulting N-density PSD is also bimodal with a large peak around 5–10 μm, and a second one around 65 μm. We argue that the relatively small number of very large particles has a limited effect on the overall optical properties of the ash within the FOV of the OP-FTIR instrument, especially for dilute plumes, and that the comparatively large number of finer particles dictates the shape of the overall extinction profile. Therefore, we believe the N-density PSD is more directly comparable with the sizes retrieved in this work, as the strongest effects on the overall shape of the particle extinction coefficients from Mie scattering largely depend on the number density of particles with diameters close to that of the measured wavelength (i.e., 8–12 μm, see Figure 5).

The chemical composition of several crystalline phases, as well as the glass matrix as determined *via* EMPA analysis are presented in Table 2. The glass composition represents a basaltic trachyandesite, and the main crystalline phases are olivine (Ol), clinopyroxene (Cpx) and plagioclase (Plag). Using the backscattered images from the EPMA analysis, we estimated the relative surface area fractions for each phase (Glass: 60%; Ol: 5%; Cpx: 10%, Plag: 25%) and used these relative fractions to calculate an approximate bulk composition for the sample. This bulk composition (a trachybasalt with ~51 wt% SiO<sub>2</sub>) was used to

parameterize the refractive index of the ash during the retrieval (see sect. 2).

### 3.2 Spectral fits

Figure 7 illustrates typical results of individual fits for selected spectra. Over the broad fitting window, the radiance difference spectra are dominated by a broadband contour representing the water vapour continuum. This contour can be positive or negative in absolute value, representing either an increase or a decrease in total water vapour column between the plume and clear sky measurements. The dashed line in the top panel of each figure emphasises this effect and shows the expected difference before considering the contributions from the plume. It is obtained by computing the radiance difference using best-fit parameters for water vapour scaling and observer temperature only and omitting all plume species. The shape of this baseline spectrum at the start of measurements depends on the respective positions of the line-of-sight between clear sky and plume and should approach zero for a clear sky taken at the plume location. Note that this radiance difference already contains recognisable spectral features for H<sub>2</sub>O (continuum and narrow absorption/emission lines), O<sub>3</sub> and CO<sub>2</sub> resulting from the overall change in total atmosphere transmission when simply moving the line-of-sight of the instrument. In Figure 7A, showing a spectrum acquired in 2019, O<sub>3</sub> (1,000–1,080 cm<sup>-1</sup>) and CO<sub>2</sub>

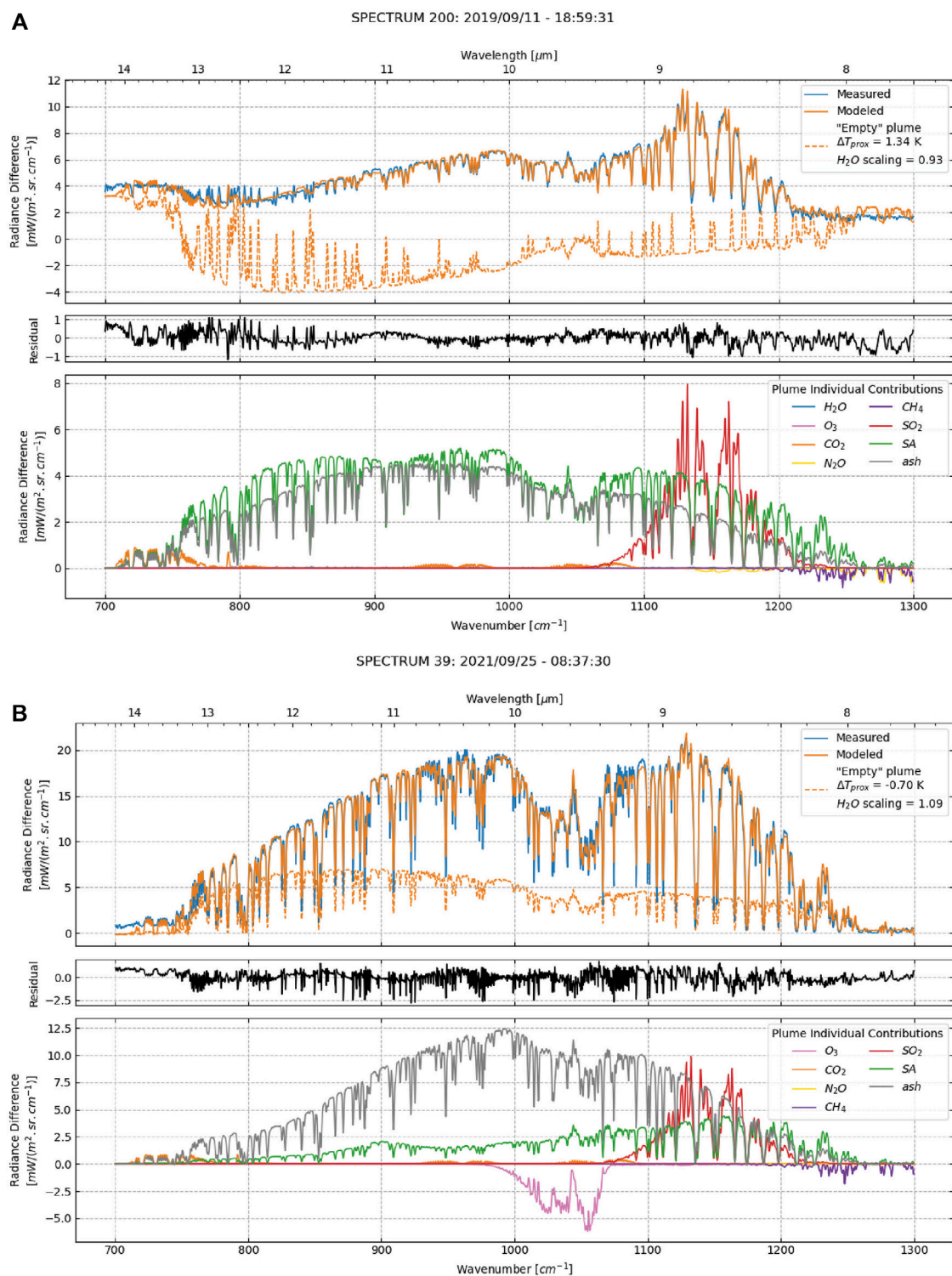
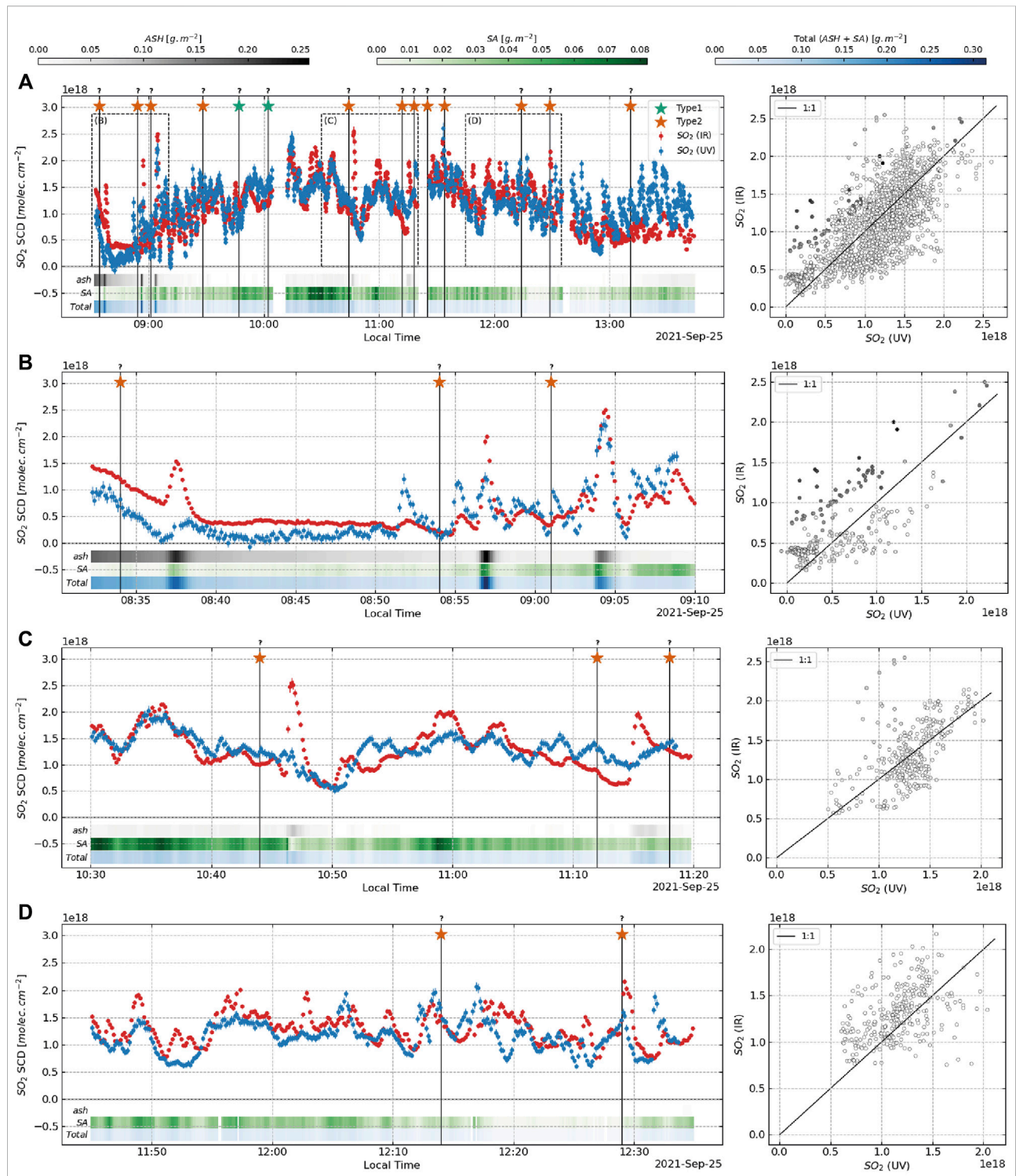


FIGURE 7

Example of fit results for selected individual spectra. In each subpanel: the top plot shows the measured [blue] and modelled [orange] spectra, along with the expected radiance difference without a plume in the line of sight [dotted orange] based on best-fit parameters for water vapour scaling and observer temperature; the middle plot shows the residual between modelled and measured spectra [black]; and the bottom plot shows the individual contribution of each plume species to the modelled spectrum (A) Plume spectrum with both ash and sulphate aerosol (SA) particulates, highlighting the differences in spectral shape between the two species, acquired on 11 September 2019 (B) Ash-rich plume spectrum acquired on 25 September 2021. Note the large  $\text{O}_3$  adjustment needed to fit the depth of the measured absorption feature.



**FIGURE 8**

Time series of  $\text{SO}_2$  SCDs measured on 25 September 2021. SCDs retrieved from the IR dataset are shown in red. SCDs retrieved from UV measurements are shown in blue. The UV time series was resampled after cross-correlation and has been shifted by 71 s to correct for the misalignment between the telescopes. Also shown are the mass SCDs for ash [grey], sulphate aerosols [SA, green] and total particulates [blue]. Stars represent individual events, recorded at the time when a plume is visible over the crater rim in video footage. Inset on the right shows a scatter plot between UV and IR SCDs, and the datapoints are coloured according to the retrieved ash SCD. Time and y-axis scales change between panels, but colour scales remain the same (A) Full dataset. Zoom windows for subsequent panels are shown as dashed boxes. Note that systematic disagreement between UV and IR retrieval occur towards the beginning and end of the measurement periods (B) Zoom window showing three ash-

(Continued)

**FIGURE 8 (Continued)**

bearing events between 08:30 and 09:10. Most data points departing from the 1:1 line on the scatter plot are associated with higher ash burdens. Note the relatively high ash burden during the first 7–8 min leading to the first ash event and the corresponding disagreement between UV and IR retrievals during that period (C) Zoom window showing two ash-bearing events between 10:30 and 11:20. Note that relatively high SA SCDs before the first event do not lead to significant disagreement between UV and IR retrievals (D) Zoom window with no ash-bearing event between 11:45 and 12:35. Note the change in scale in the ash SCD colour scale.

(925–1,000  $\text{cm}^{-1}$ ) appear as emission lines (due to the reduced transmission associated with a  $\text{H}_2\text{O}$  scaling factor  $<1$ ), and the baseline minimum value goes from  $-1$  to  $-6 \text{ mW}/(\text{m}^2\text{-sr}\cdot\text{cm}^{-1})$  over the course of  $\sim 30$  min. This value is expected to gradually change over the course of measurements, as the background atmospheric conditions evolve. In contrast, [Figure 7B](#) shows a spectrum acquired in 2021, where the baseline is a positive radiance difference ( $\text{H}_2\text{O}$  scaling factor  $>1$ ) and  $\text{O}_3$  and  $\text{CO}_2$  appear as absorption features. The fitting window was deliberately chosen to include areas on either side where the atmosphere is virtually opaque ( $<730 \text{ cm}^{-1}$  and  $>1,270 \text{ cm}^{-1}$ ). The radiance at those wavelengths represents the blackbody emission at the temperature of the most proximal layer, and we can use the value of the radiance difference to retrieve the temperature of the proximal layer (layer 1).

The bottom panel in each figure shows the contributions of each plume species (including the ad hoc corrections for atmospheric gases) superimposed over the baseline radiance difference. Each individual contribution is computed using the forward model and zeroing all quantities within the plume except for the species of interest. Note that because the background and foreground atmosphere are always an inherent part of the forward model, water vapour absorption lines still appear in the contribution from each individual species. The most instantly recognisable feature is the emission associated with  $\text{SO}_2$ . In particulate-rich spectra, a strong  $\text{O}_3$  absorption is visible, related to the severe decrease in transmission introduced by the heavy particle burden and often requiring an ad hoc correction.

### 3.3 Side-by-side IR and UV measurements

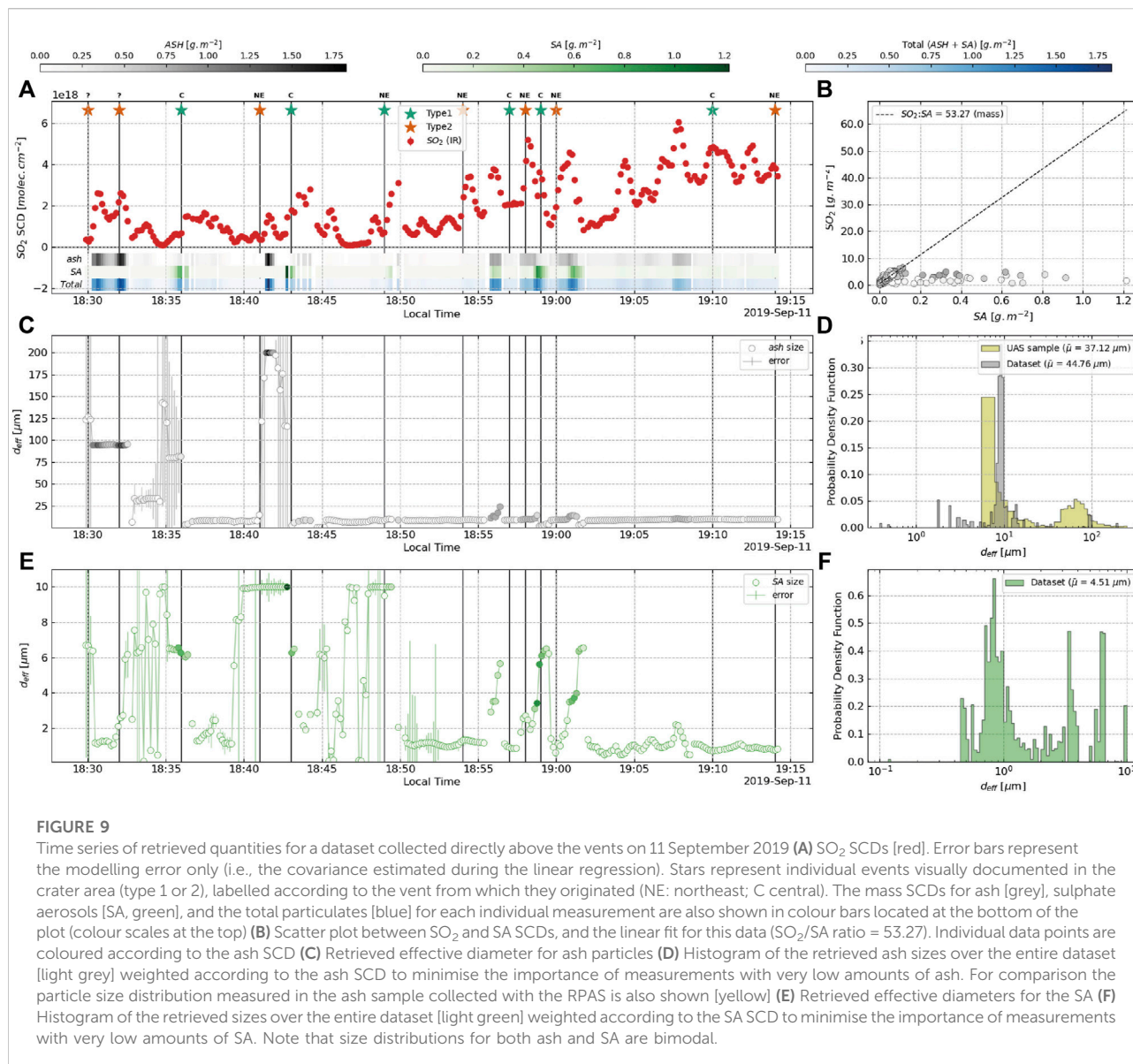
[Figure 8](#) shows the time series of  $\text{SO}_2$  SCDs retrieved from our FTIR measurements for one dataset acquired during our second measurement campaign in 2021. We also present  $\text{SO}_2$  SCDs measured using a co-located UV spectrometer. Disagreement in both absolute values of the SCD and timing of individual peaks are to be expected. They may arise as a consequence of differences in a series of factors between the two methods, such as: 1) the size of the respective FOVs ( $.03$  rad for the IR,  $.1$  rad for the UV); 2) the alignment of the telescopes; 3) the integration time ( $0.2$  s in the UV,  $8.9$  s in the IR); and 4) different random and systematic error sources between the two methods. The UV time series was smoothed using a kernel of

length equal to the IR integration time and resampled to match the temporal x-axis in the IR time series. Moreover, we determined the optimal lag using a cross-correlation method and shifted the UV time series accordingly. We would expect this lag to vary over the course of the measurements, as it is tied to the plume velocity, and plumes associated with crater explosions will travel at greater velocities. However, we found that an overall lag of  $\sim 71$  s resulted in a good match between the timing of the main events. Retrieved SCDs between the IR and UV measurements generally agree within a factor of  $\sim 2$  (scatter plot in [Figure 8A](#)). The main discrepancies occur towards the beginning and end of datasets with the IR method retrieving systematically lower SCDs than the UV method at the beginning of the dataset in [Figure 8A](#), and systematically higher SCDs towards the end of the dataset.

[Figure 8](#) further documents explosive events, as recorded in GoPro time-lapse footage (orange stars). Here we only report ash explosions, defined as type 1 events following the terminology in [Patrick et al. \(2007\)](#), and mark them at the time of their first appearance above the crater rim from our vantage point. Type 2 events (essentially bubble bursts associated with ballistics) were much more difficult to identify from the 2021 vantage point without a direct view of the craters ([Figure 1](#)). It is also impossible to assign a specific crater of origin for individual events for the 2021 time series. All documented events are followed by a marked increase in retrieved  $\text{SO}_2$ , SA and ash contents, after a delay of 1–2 min representing the time needed for the plume to move into the FOV of the instruments.

### 3.4 Near-vent measurements

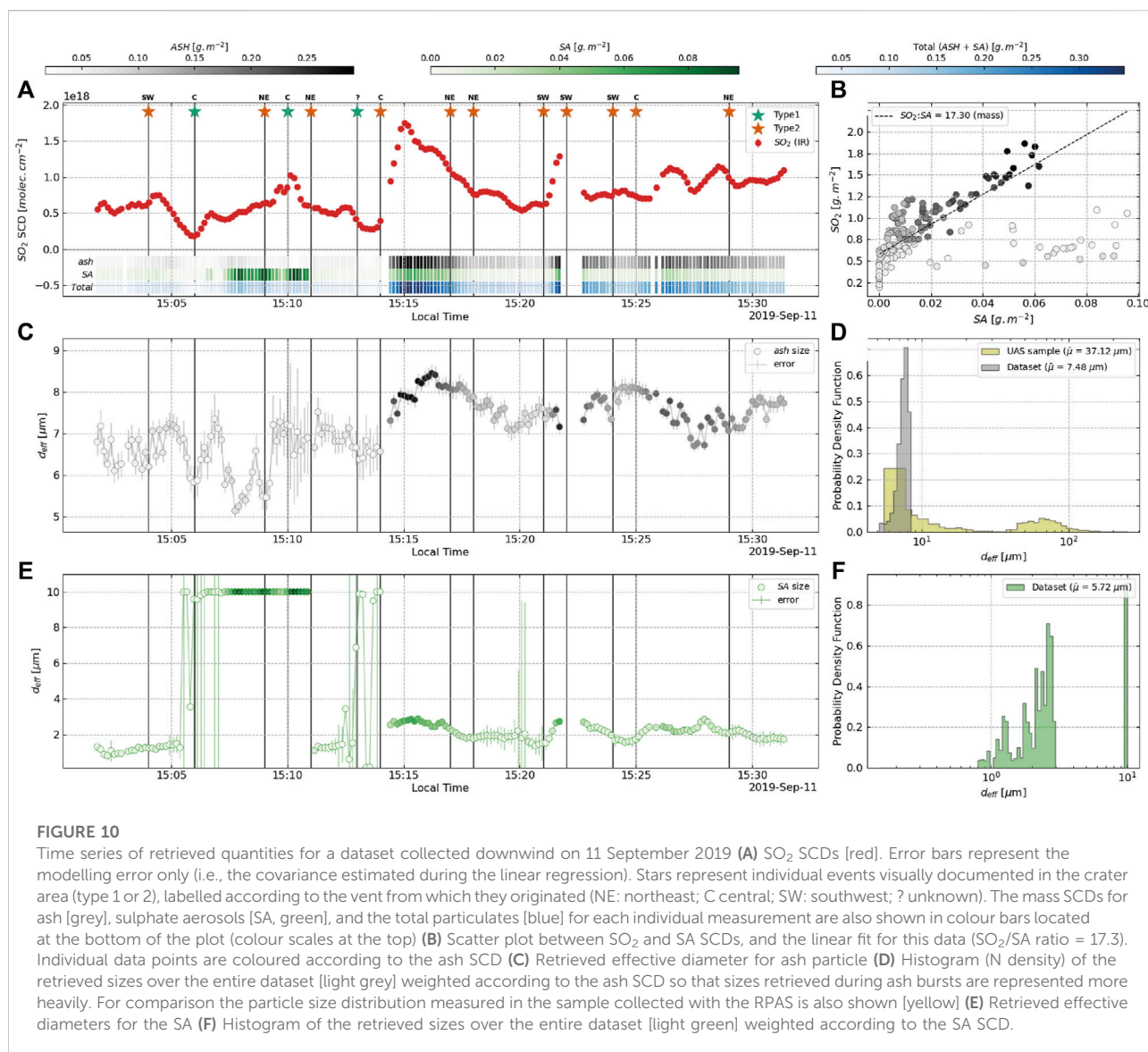
During the 2019 campaign, we performed measurements from the l'Osservatorio restaurant, with a direct view of the crater area ([Figure 1B](#)). We were able to move the FOV of the instrument to intersect the plume directly above the vent. A time series of the retrieved quantities for a dataset collected in this configuration is shown in [Figure 9](#). During this period, we captured the baseline passive degassing plume, as well as plumes resulting from explosive events. Events were documented through visual observation and logged manually. As we had a direct view of the crater area, the explosive plumes can be separated into two classes with relation to the event types defined by [Patrick et al. \(2007\)](#). Type 1 events (bubble bursts + ballistics) produce plumes with low ash content and elevated concentrations of  $\text{SO}_2$  (green



stars). Type 2 events, on the other hand, are ash-rich with a visibly dark plume (orange stars). The FOV of the instrument was positioned directly above the NE crater area. As a result, this dataset mainly contains events originating from the NE and central vents (which were directly behind the NE vents along the line of sight). Some emissions from the SW crater area may have entered our FOV but, given the wind direction during our measurements, this was challenging to determine visually. Type 1 events originated from both NE and C areas, and type 2 events mainly originated from the NE craters. Absolute retrieved SCDs for SO<sub>2</sub>, ash and sulphate aerosols above the vents are relatively high (peak SO<sub>2</sub>:  $6 \times 10^{18}$  molec·cm<sup>-2</sup>, peak ash: 1.75 g·m<sup>-2</sup>, peak SA: 1.2 g·m<sup>-2</sup>). Peaks in SO<sub>2</sub> within the time series generally occur shortly

after the onset of each event. Retrieved SA particle sizes are shown in the bottom plot in Figures 9E, F. The probability density function, where each measurement of particle size is weighed according to the associated SCD, exhibits a mode around 0.8 μm, representative of the typical size retrieved during low level degassing (mean  $d_{eff}$  value of  $1.79 \pm 3.08$  μm). There are also several peaks at higher diameters, representing  $d_{eff}$  values retrieved during the explosive events (i.e., type 2 ca 18:56, 18:58 and 19:02 and type 1 ca 18:36 and 18:43, Figure 9E).

In a scatter plot between SO<sub>2</sub> and SA over the entire dataset (Figure 9B), the measurements with lower amounts of particulates (light shades) define a ratio line. We calculate SO<sub>2</sub>/SA mass ratios using a robust linear regression (Siegel,



1982) which emphasises the overall trend rather than more extreme data points, in order to minimise the effects of those measurements with high amounts of particulates during the explosive events. This is done so we can quantify the sulphur partitioning in the gas plume during passive degassing periods. We observe a ratio of  $\sim 53$  by mass in this dataset. Values from similar datasets range between 40 and 80.

Retrieved ash particle sizes are shown in the middle plot in Figures 9C, D. The retrieved size for ash particles increases during explosive events. The probability density function exhibits a clear mode at  $\sim 10 \mu\text{m}$  during non-explosive phases (range between 5 and  $15 \mu\text{m}$ ). During the most intense ash-rich type 2 events (e.g., ca 18:30–18:33 and ca 18:42 in Figure 10), ash  $d_{\text{eff}}$  reaches much higher values, up to  $200 \mu\text{m}$ , the upper bound for ash size set in the algorithm.

During type 2 events of lower intensity (e.g., three events in quick succession ca. 18:56, 18:58 and 19:00), particle size also increases during each event, but to lower values of  $10\text{--}30 \mu\text{m}$ .

### 3.5 Downwind measurements

Figure 10 shows a time series of measurements acquired from the same vantage point and on the same day (11 September 2019) as those measurements shown in Figure 9, but where the instrument FOV intersected the plume  $\sim 0.8 \text{ km}$  downwind (Figure 1B). The measured SCDs for all target species (peak SO<sub>2</sub>:  $2 \times 10^{18} \text{ molec}\cdot\text{cm}^{-2}$ , peak ash:  $.3 \text{ g}\cdot\text{m}^{-2}$ , peak SA:  $.1 \text{ g}\cdot\text{m}^{-2}$ ) are lower than in the near-vent measurements, representing the dilution of the plume and loss processes (e.g., SO<sub>2</sub> oxidation and

settling of PM) as it travels. Wind speed on that day was relatively low, and this distance corresponds to a plume age of approximately 3–5 min. Recorded type 1 and type 2 events at the vents appear disassociated with peaks in the SO<sub>2</sub> time series. However, we identify three individual events within the time series: one event with elevated SO<sub>2</sub> and SA, with a slow onset at ca. 15:07, assumed to be a type 2 event), and two events with sharper onsets at ca. 15:14 and 15:21 showing elevated SO<sub>2</sub>, SA and ash contents (assumed to be type 2 events). The mean SO<sub>2</sub>/SA mass ratio for this particular dataset is ~17, and values for downwind datasets range between 10 and 30.

Retrieved sizes for the SA downwind are  $5.21 \pm 4.27 \mu\text{m}$  during low level degassing, and  $2.19 \pm 0.36 \mu\text{m}$  on average during explosive events (type 1 and type 2). Sizes retrieved during a type 1 event with a high SA SCD (ca 15:07–15:10 in Figure 10) show elevated values, reaching the upper bound for SA size set in the algorithm ( $10 \mu\text{m}$ ). Retrieved sizes for ash in the downwind dataset are  $6.66 \pm 0.57 \mu\text{m}$  outside of ash-rich events, and  $7.68 \pm 0.38 \mu\text{m}$  during ash-rich events. Both values are in good agreement with the smaller mode of the particle size distribution found in our collected sample (Figure 6).

## 4 Discussion

### 4.1 Sensitivity to plume temperature

The principal source of uncertainty in the method comes from the estimation of plume temperature in the FTIR forward model. This is illustrated by systematic disagreements between the UV and IR retrievals of SO<sub>2</sub> SCDs towards the beginning and end of datasets (see Figure 8A). As the measurement period evolves, the actual temperature at plume height increases or decreases (depending on time of day), while the assumed plume temperature in our model remains the same (extracted from the reference atmospheric sounding, which is taken only in 12 h intervals, and at a location >100 km away from the measurement location). If the assumed temperature is colder than the plume actually is, the amount of SO<sub>2</sub> retrieved by our method will be an overestimate of the actual SO<sub>2</sub> in the plume. Conversely, if the assumed temperature is warmer than the actual temperature, our measurements will be an underestimate. UV spectroscopy is not affected by this assumption and thus differences may arise between the retrieved quantities from the FTIR and the UV measurements. A further complication is that both plume height and atmospheric temperature at plume height may vary over the course of the measurements, leading to systematic errors in all quantities retrieved by the method. As the radiance difference is calculated using a clear sky spectrum acquired at the beginning or end of the measurements, exacerbating the differences in measured radiance which result from changing atmospheric

conditions in spectra collected further away from the calibration period, using more frequent clear sky measurements will yield more consistent results. In addition, plume temperature might be higher due to the presence of the volcanic plume, i.e., the actual temperature in layer 2 may differ from the one recorded in the atmospheric profile due to the hot volcanic gas and particles.

To quantify the error linked with the plume layer temperature, we introduced a fixed temperature difference ( $\Delta t_{\text{plume}}$ ) between the temperature in the volcanic layer at the time of measurement and the clean air layer temperature in the clear sky measurement and performed the retrieval on a subset of 1,000 measurements from 25 September 2021, for various values of  $\Delta t_{\text{plume}}$  (Figure 11). The temperature of the plume at Stromboli is frequently recorded using a Multi-component Gas Analyser System (Multi-GAS) at the summit (Aiuppa et al., 2009; Aiuppa et al., 2010). Although temperature measurements are not reported in published studies, they are recorded by the instrument and typically fall within 1–3 degrees of the ambient temperature when the plume drifts over the summit (INGV personal communication). Therefore, we vary  $\Delta t_{\text{plume}}$  between values of  $-5 \text{ K}$  and  $+5 \text{ K}$ . In addition, we ran the retrieval on the same data subset leaving the temperature of the volcanic layer as a free parameter. This latter approach yielded unrealistic results, with  $\Delta t_{\text{plume}}$  ranging from  $-30 \text{ K}$  to  $+30 \text{ K}$  within the same dataset, leading to overestimates of up to a factor of four in the retrieved SO<sub>2</sub> SCD in spectra with the highest amounts of particulates. However, these results allow us to quantify the expected errors related to plume temperature. When plotting the ratio between the SO<sub>2</sub> SCD retrieved with a free  $t_{\text{plume}}$  and the SO<sub>2</sub> SCD retrieved with a fixed  $t_{\text{plume}}$  against the associated  $\Delta t_{\text{plume}}$ , they outline a very clear relationship, which can be approximated using an exponential decay function. We estimate that uncertainties in assumed plume temperature will lead to errors in the retrieved SO<sub>2</sub> SCDs of a factor of ~3.5% per K. When considering a realistic range of assumed plume temperatures, this translates to overestimates of up to 19% ( $\Delta t_{\text{plume}} = -5 \text{ K}$ ) and underestimates of up to 16% ( $\Delta t_{\text{plume}} = +5 \text{ K}$ ). Measurements with high SCDs of particulates depart from this overall relationship and introduce larger overestimates. Similar values are found when examining other retrieved quantities (summarised in Table 3). These uncertainties are much larger than the typical fitting error of ~2.2% and represent the largest limitation in the method. Local measurements of temperature at plume height and accurate visual determination of the plume height will help mitigate the potential for error.

### 4.2 Plumes with high optical thickness

Previous measurements have shown the PM-related optical properties of the Stromboli plume to vary with the occurrence of

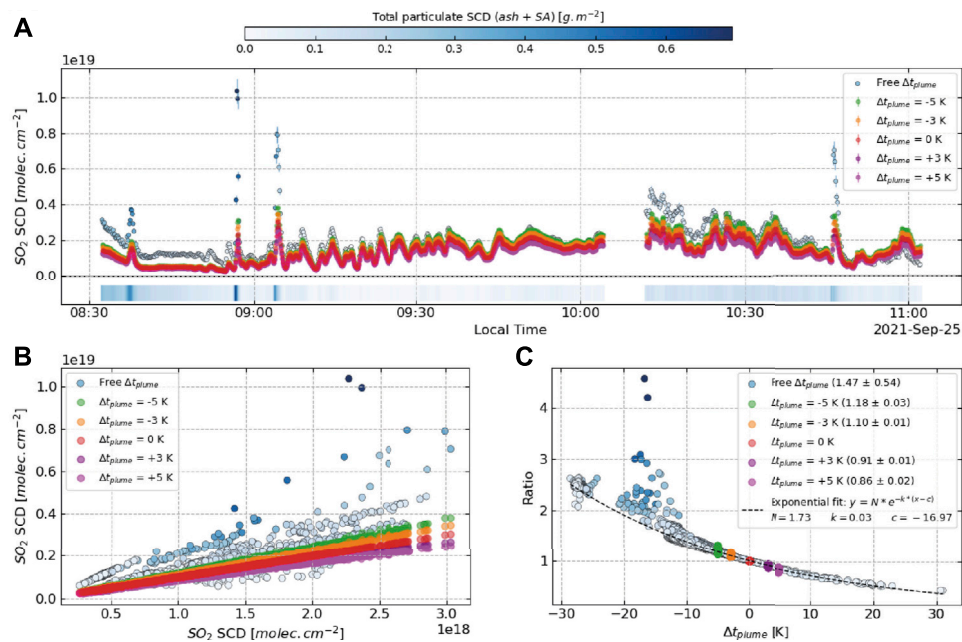


**FIGURE 11**

Sensitivity analysis of the effect of plume temperature on the retrieved  $\text{SO}_2$  SCDs. **(A)** Time series of  $\text{SO}_2$  SCDs for a subset of 1,000 spectra measured on 25 September 2021, using various values of  $\Delta T_{\text{plume}}$  (green:  $-5$  K; orange:  $-3$  K; red:  $0$  K; purple:  $+3$  K; magenta:  $+5$  K; blue: free parameter). Bar plot at the bottom shows the total SCD for all particulate species (colour scale at the top), highlighting the eruptive events with high ash or sulphate aerosols (SA). Data points in the free  $T_{\text{plume}}$  retrieval are also coloured according to the total particulate SCD **(B)** Retrieved  $\text{SO}_2$  SCDs for each of the time series mentioned above against the corresponding  $\text{SO}_2$  SCD in the reference retrieval ( $\Delta T_{\text{plume}} = 0$  K). Note that measurements with high amounts of particulates produce larger overestimates in the retrieved  $\text{SO}_2$  **(C)** Ratio between retrieved  $\text{SO}_2$  in each time series against the reference retrieval ( $\Delta T_{\text{plume}} = 0$  K). Measurements with low particulate content outline an exponential relationship, with an expected uncertainty of  $\sim 3.5\%$  per K.

**TABLE 3** Estimated errors associated with plume temperature. Expressed as the ratio of the retrieved SCD over a reference dataset with  $\Delta T_{\text{plume}} = 0$  K.

$\Delta T_{\text{plume}}$	$\text{SO}_2$ error	SA error	Ash error
$-5$ K	$1.18 \pm 0.03$	$1.18 \pm 0.05$	$1.04 \pm 0.07$
$-3$ K	$1.10 \pm 0.01$	$1.11 \pm 0.03$	$1.03 \pm 0.04$
$+3$ K	$0.91 \pm 0.01$	$0.91 \pm 0.02$	$0.97 \pm 0.03$
$+5$ K	$0.86 \pm 0.02$	$0.86 \pm 0.03$	$0.915 \pm 0.04$

individual events (Sellitto et al., 2021). Our results further support these observations, with type 1 events generally associated with a peak in  $\text{SO}_2$  SCD, and an increase in SA SCD, whereas type 2 events are associated with increased amounts of both ash and SA SCD (Figure 9). Some type 1 and type 2 events were not accompanied by particle increases and in one case no  $\text{SO}_2$  peak was observed. This may reflect the fact that some plumes drifted above the FOV of our instrument, either because the explosion that produced them injected significant momentum into the plumes, or because shifts in wind direction or speed caused the plume to rise more vertically in some cases than others. As the dataset shown in

Figure 9 was acquired in the run up to sunset (approximately 19:15 local time), it is also possible that our manual observations are incomplete or inaccurate, particularly towards the end of the dataset as it became darker.

The presence of high amounts of particulates within a plume (e.g., ash-bearing plumes after explosions or those with a high optical thickness due to large amounts of aerosols) can negatively affect UV measurements and lead to large errors in retrieved  $\text{SO}_2$  SCDs if realistic radiative transfer is not taken into account (Kern et al., 2010; Kern et al., 2012; Kern et al., 2013; Varnam et al., 2020). Although both over- and underestimations are possible, depending on the specific conditions within a plume (i.e., magnitude of the  $\text{SO}_2$  column amounts and nature of the scattering aerosol), underestimates are more likely in plumes with high optical thicknesses, particularly if the particulate species within the plume also exhibit strong absorbing properties, as is the case for ash-laden plumes captured close to the vent (Kern et al., 2013). In such cases, IR retrievals may offer an advantage, as they are less likely to be impacted by multiple scatterings (typical sizes for volcanic particles are often much smaller than the  $8\text{--}12$   $\mu\text{m}$  wavelength range of the method) and by light dilution effects. Our method offers a means of quantifying the aerosol optical thickness and  $\text{SO}_2$  SCDs from a

**TABLE 4 Sulphur speciation in proximal volcanic plumes from this and previous studies.**

Volcano	Study	SO <sub>2</sub> /SA (mass)	SO <sub>4</sub> <sup>2-</sup> /SO <sub>2</sub> (molar)
Masaya	Allen et al. (2002)	95–1,200	0.04–0.4 <sup>a</sup>
	Mather et al. (2003a)	25 <sup>a</sup>	0.01
	Sellitto et al. (2019)	400	0.15 <sup>a</sup>
Vulcano	Mather et al. (2004a)	100 <sup>a</sup>	0.04
Lascar	Mather et al. (2004b)	25 <sup>a</sup>	0.01
Villarica	Mather et al. (2004b)	50 <sup>a</sup>	0.02
Etna	Roberts et al. (2018)	38 <sup>a</sup>	0.015
Stromboli	This study	53	0.021

<sup>a</sup>Converted from originally reported value assuming SA, acidity of 65 wt. % H<sub>2</sub>SO<sub>4</sub>.

single measurement. For optically thick plumes containing very large amounts of ash or PM, underestimates in our IR retrievals should still be expected, as the radiance collected at the instrument would originate mainly from the surface of the plume. However, for moderate particle concentrations, our method offers a way to compensate for the expected loss of radiance from within the plume layer. This is apparent at several points in the time series presented in Figure 8 and highlighted in subpanels B–C, where ash-rich plumes are generally associated with higher retrieved SO<sub>2</sub> SCDs in the IR, by factors ranging from 2 to 5. We propose that this represents an underestimate of the true SO<sub>2</sub> burden by the UV method, and that the SCDs retrieved in the IR are closer to the concentrations within the plume at the time of measurement. Alternatively, it is possible that plumes with high amounts of ash retain heat more efficiently, and as a result the assumption of a plume in thermal equilibrium with the atmosphere is no longer valid. In such a case, the retrieved SO<sub>2</sub> SCD with the IR method would constitute an overestimate of the real values, as warmer plumes emit more radiation. These discrepancies merit further investigation within a dedicated, systematic side-by-side experiment in which multiple scattering and light dilution effects are accounted for in both UV and IR retrievals.

### 4.3 Sulphur speciation during plume transport

Table 4 summarises sulphur speciation values previously reported and measured in proximal plumes (<1 km from source) at Stromboli and elsewhere. Sulphur partitioning between the gas and aerosol phases is generally reported as the molar ratio of SO<sub>4</sub><sup>2-</sup> ions to SO<sub>2</sub> (SO<sub>4</sub><sup>2-</sup>/SO<sub>2</sub>) when measured with filter packs. Alternatively, when retrieved with spectroscopic techniques, the reported value is often the mass ratio of the gas phase over the aerosol phase, including the water (SO<sub>2</sub>/SA). The conversion between the two values depends on the

acidity of the aerosols themselves, which is not always reported. For a simple comparison, we assume an acidity of 65 wt% H<sub>2</sub>SO<sub>4</sub> (the value used to generate our reference extinction spectra), and present both ratios. The SO<sub>2</sub>/SA measured in our near-vent measurements is on the lower side of the range observed in proximal plumes at other volcanoes, suggesting the presence of large amounts of primary sulphate aerosols (i.e., those condensed directly from the high-temperature gas emitted from the magma) in the passive plume and during type 1 events (which typically have lower particulate loads than type 2 events). Alternatively, this could reflect the rapid formation of sulphate *via* oxidation of SO<sub>2</sub> condensing onto the primary particles in the plume or a higher water content of the SA in our measurements. This is supported by the observations that the sizes measured here (Figure 9) are rather large compared to those expected for newly formed particles (<1 μm for particles within the “nucleation mode”) (Whitby, 1978; Mather et al., 2003b).

SO<sub>2</sub>/SA ratios in diluted downwind datasets (range 10–30, mean of ~17 in the dataset illustrated in Figure 10) are lower than those found near-vent (range 40–80, mean of ~53 in the dataset illustrated in Figure 9), suggesting either an increase in sulphate aerosol mass and/or a decrease in SO<sub>2</sub> mass as the plume ages. Several mechanisms exist which could explain the observed decrease in SO<sub>2</sub>/SA ratio with plume age. SO<sub>2</sub> depletion by oxidation into sulphuric acid is a commonly proposed mechanism (Eatough et al., 1994) and has been documented in volcanic plumes, with SO<sub>2</sub> loss rates in tropospheric plumes ranging between 10<sup>-7</sup> and 10<sup>-3</sup> s<sup>-1</sup> (Oppenheimer et al., 1998b; McGonigle et al., 2004; Rodríguez et al., 2008). As SO<sub>2</sub> is oxidized, the decrease in SO<sub>2</sub>/SA ratio then results from both a loss of gaseous SO<sub>2</sub> in the plume, and from condensation of sulphate formed as SO<sub>2</sub> is oxidized, either increasing the size of existing particles, or nucleating new particles, and ultimately causing an increase in aerosol mass. However, even assuming a fast depletion rate at the upper bound of the range documented above (10<sup>-3</sup> s<sup>-1</sup>), it is not clear that this oxidation process would be fast enough to explain the changes observed here, which took

place over distances of <1 km and for plume ages of only a few minutes. Alternatively, the mass of SA may also be increased by condensation of water into the aerosol, a process by which the existing sulphate aerosols lower the supersaturation threshold required to grow droplets (Mather et al., 2004a; Mather et al., 2004b), potentially ultimately acting as seeds for the formation of clouds (Pianezze et al., 2019). This process would increase the overall mass of the SA while decreasing their relative acidity. Given the fixed parameter for SA acidity in our retrieval, our model is not able to measure this change in acidity. However, hygroscopic growth is consistent with both the slight increase in retrieved SA size (during periods of passive degassing) and the decrease in SO<sub>2</sub>/SA mass ratio in the downwind measurements and is therefore a plausible mechanism to explain our observations. Two recent studies have investigated the evolution of SO<sub>2</sub> and SA in the Stromboli and Etna plume (Pianezze et al., 2019; Sahyoun et al., 2019). Both studies found an increase in the number concentration of SA particles with distance from the vent, combined with an increase in the size of the measured particles. Although the mechanisms investigated by these studies take place over much larger distances and targeting older plumes, their interpretations are broadly consistent with our observations, and suggest the mechanisms of particle growth that ultimately can result in cloud condensation occur even in very young plumes such as those we measured. Further investigation of these mechanisms might elucidate volcanic impacts and interactions with cloud cover in the troposphere (e.g., Ebmeier et al., 2014).

#### 4.4 Ash settling during plume transport

As mentioned previously, the sensitivity of the retrieval to particle sizes above 20 μm is not well established, and it is possible that the retrieved values do not represent the true size within the plume. Nevertheless, our observations of significant increases in optical depth in the long-wave infrared spectrum and rapid shifts in particle size during type 2 events are consistent with the increase in aerosol optical depth and decrease in the Angstrom exponent observed at shorter wavelengths by Sellitto et al. (2021) and are the likely result of an injection of coarser particles from the explosions. Sizes retrieved over the entirety of the dataset capture the full range of ash particle sizes found in the sample collected with the RPAS, with the fine fraction often found during low-level degassing and the coarser particles during type 2 events.

The size of ash retrieved in diluted plumes (either downwind or above the vent during non-explosive activity) is remarkably consistent, with values of 5–10 μm in both datasets. This value is also consistent with the fine size fraction in our collected sample. Coarser particles (65–200 μm) retrieved from near-vent measurements are not detected in the downwind measurements, even when a high SCD of ash is retrieved,

suggesting that they have already been removed by sedimentation at that point. This is consistent with our visual observations during the measurement period of large “fingers” of ash raining from the drifting plumes and depositing the coarser particles on the slopes of the volcano, as documented in Freret-Lorgeril et al. (2020). It is also consistent with the observations of Sellitto et al. (2020) who found a decrease in aerosol size with increasing distance from the vent in the proximal (<20 km) plume at Etna volcano, which they interpreted as due to the sedimentation of ash (and possibly coarser SA). It should be noted that the sensitivity of the IR retrieval to particle size is most pronounced in the range of particle sizes 1–10 μm, where the size of the particles approaches the wavelength of radiation. The spectral shape for ash shows relatively little variation with increasing sizes above 20 μm (see Figure 5), and the detection of coarser particle sizes in this work should be taken as an indication of their presence rather than an accurate determination of their actual size.

## 5 Conclusion and future work

Here we present a new method for simultaneous quantification of gases and particulates in volcanic plumes using emission OP-FTIR measurements. Using a broad fitting window, the method allows for identification and quantification of ash and sulphate aerosols within a plume, and the determination of particle size. Retrieved SO<sub>2</sub> column densities are in reasonable agreement (within a factor of 2) with those retrieved using UV spectroscopy with the larger discrepancies occurring during ash-rich events. SO<sub>2</sub> SCDs retrieved with the IR method are generally larger than those retrieved with traditional UV methods. The ability to measure particles and gas simultaneously could prove useful in understanding and quantifying the underestimation of SO<sub>2</sub> column densities by UV methods which results from multiple scattering, either in plumes containing large amounts of particulates or when measurements are performed from large distances (e.g., Kern et al., 2013; Campion et al., 2014; Varnam et al., 2020). This invites further investigation of ash- and SA-rich plumes using simultaneous measurements with both methods.

Using this new methodology, we document the plume composition during different types of volcanic activity at Stromboli (passive degassing, type 1 ash-poor and type 2 ash-rich explosions) and its evolution over a short distance downwind of the active vent. Our algorithm consistently identifies a fine ash fraction (5–10 μm) present even during non-explosive phases and in distal plumes, as well as coarser ash particles (30–200 μm, ~65 μm mean) found only in datasets collected near the vent after type 2 events. We collected an *in-situ* sample of ash during an explosive event using a Remotely Piloted Aircraft System (RPAS), allowing us to compare particle sizes measured remotely with those found directly within the plume.

Both size modes detected by our FTIR method were found in the RPAS sample, providing validation for the retrieval algorithm. The measured loss of the coarse ash size at a short distance (~8 km) from the vent is consistent with visual observations of particle settling below the drifting plume. Measurements of SA size (slightly coarser particles found in downwind datasets) and SO<sub>2</sub>/SA mass ratios (from 53 near the vent to 17 downwind) suggest rapid aerosol growth over these short distances as well, which we propose to be dominated by water uptake. Long-term deployment of this method might provide useful additional metrics alongside a baseline of SO<sub>2</sub> data to investigate physical and chemical processes occurring within tropospheric plumes over short (1–10 km) distances. Emission IR measurements also enable measurements during periods when UV methods cannot be used (i.e., at night) and without the need to align the spectrometer with an IR source, opening the possibility for flexible 24 h gas monitoring.

Given the encouraging results reported here, we suggest the method should be further developed to explore its full potential. Future work will focus on longer term deployment at Stromboli and other volcanoes, with the aim of creating time series spanning days or weeks, and to evaluate the usefulness of the method for continuous monitoring. As well, systematic comparison with UV retrievals should be explored, with the aim of improving SO<sub>2</sub> quantification in particulate-rich plumes. Finally, a number of improvements and extensions should be tested and implemented within the source code: 1) fitting of individual absorption lines for gases such as CO<sub>2</sub> following the method outlined in Goff et al. (2001); 2) quantitative retrieval of SiF<sub>4</sub>; 3) improved spectral fits focused on the particulate species using spectral micro-windows in order to alleviate the effects of water vapour absorption; and 4) exploring the evolution in aerosol composition by fixing the particle size and targeting SA particle composition, including the possibility of sulphate-coated ash particles.

## Data availability statement

The raw data supporting the conclusions of this article will be made available by the authors, without undue reservation.

## Author contributions

J-FS designed and supervised the measurement campaigns, developed the algorithm, processed the data and wrote the manuscript first draft. TM and MB supervised all work, participated in field campaigns and

assisted in the development of the algorithm. AS provided the OP-FTIR instrument, assisted in data collection and analysis. BE and MV assisted in the collection and analysis of UV measurements, RG advised on the implementation of the quantitative retrieval for particulates. All authors edited the manuscript.

## Funding

The work outlined in this manuscript was supported by NERC award NE/S004025/1.

## Acknowledgments

The authors would like to thank INGV-Catania, and particularly Giuseppe Salerno, for facilitating access to Stromboli volcano during the field campaigns and for loaning UV equipment. We would also like to thank Evgenia Ilyinskaya for her help in the PSD analysis of the ash sample, Zoltán Taracsák for performing the EMPA measurements, and Anu Dudhia for insightful discussions about the physics behind the method and the use of the RFM software. We also thank Simon Carn, Pasquale Sellitto and Wolfgang Stremme for their insightful comments and suggestions which led to significant improvement of the manuscript. For the purpose of Open Access, the author has applied a CC BY public copyright licence to any Author Accepted Manuscript (AAM) version arising from this submission.

## Conflict of interest

The authors declare that the research was conducted in the absence of any commercial or financial relationships that could be construed as a potential conflict of interest.

## Publisher's note

All claims expressed in this article are solely those of the authors and do not necessarily represent those of their affiliated organizations, or those of the publisher, the editors and the reviewers. Any product that may be evaluated in this article, or claim that may be made by its manufacturer, is not guaranteed or endorsed by the publisher.

## References

- Aiuppa, A., Federico, C., Giudice, G., Giuffrida, G., Guida, R., Gurrieri, S., et al. (2009). The 2007 eruption of Stromboli volcano: Insights from real-time measurement of the volcanic gas plume CO<sub>2</sub>/SO<sub>2</sub> ratio. *J. Volcanol. Geotherm. Res.* 182, 221–230. doi:10.1016/j.jvolgeores.2008.09.013
- Aiuppa, A., Bertagnini, A., Métrich, N., Moretti, R., Di Muro, A., Liuzzo, M., et al. (2010). A model of degassing for Stromboli volcano. *Earth Planet. Sci. Lett.* 295, 195–204. doi:10.1016/j.epsl.2010.03.040
- Alfano, F., Bonadonna, C., Volentik, A. C. M., Connor, C. B., Watt, S. F. L., Pyle, D. M., et al. (2011). Tephra stratigraphy and eruptive volume of the May, 2008, Chaitén eruption, Chile. *Bull. Volcanol.* 73, 613–630. doi:10.1007/s00445-010-0428-x
- Allard, P., Burton, M., and Muré, F. (2005). Spectroscopic evidence for a lava fountain driven by previously accumulated magmatic gas. *Nature* 433, 407–410. doi:10.1038/nature03246
- Allard, P., Burton, M., Sawyer, G., and Bani, P. (2016). Degassing dynamics of basaltic lava lake at a top-ranking volatile emitter: Ambrym volcano, Vanuatu arc. *Earth Planet. Sci. Lett.* 448, 69–80. doi:10.1016/j.epsl.2016.05.014
- Allen, A. G., Oppenheimer, C., Ferm, M., Baxter, P. J., Horrocks, L. A., Galle, B., et al. (2002). Primary sulfate aerosol and associated emissions from Masaya volcano, Nicaragua: Primary sulfate aerosol from masaya volcano. *J. Geophys. Res.* 107, ACH 5-1–ACH 5-8. doi:10.1029/2002JD002120
- Barsotti, S., Andronico, D., Neri, A., Del Carlo, P., Baxter, P. J., Aspinall, W. P., et al. (2010). Quantitative assessment of volcanic ash hazards for health and infrastructure at Mt. Etna (Italy) by numerical simulation. *J. Volcanol. Geotherm. Res.* 192, 85–96. doi:10.1016/j.jvolgeores.2010.02.011
- Biermann, U. M., Luo, B. P., and Peter, Th. (2000). Absorption spectra and optical constants of binary and ternary solutions of H<sub>2</sub>SO<sub>4</sub>, HNO<sub>3</sub>, and H<sub>2</sub>O in the mid infrared at atmospheric temperatures. *J. Phys. Chem. A* 104, 783–793. doi:10.1021/jp992349i
- Burton, M. R., Oppenheimer, O., Horrocks, L. A., and Francis, P. W. (2000). Remote sensing of CO<sub>2</sub> and H<sub>2</sub>O emission rates from Masaya volcano, Nicaragua. *Geology* 28, 915–918. doi:10.1130/0091-7613(2000)028<0915:rsocah>2.3.co;2
- Burton, M. R., Oppenheimer, C., Horrocks, L. A., and Francis, P. W. (2001). Diurnal changes in volcanic plume chemistry observed by lunar and solar occultation spectroscopy. *Geophys. Res. Lett.* 28, 843–846. doi:10.1029/2000GL008499
- Burton, M., Allard, P., Mure, F., and La Spina, A. (2007). Magmatic gas composition reveals the source depth of slug-driven strombolian explosive activity. *Science* 317, 227–230. doi:10.1126/science.1141900
- Butz, A., Dinger, A. S., Bobrowski, N., Kostinek, J., Fieber, L., Fischerkeller, C., et al. (2017). Remote sensing of volcanic CO<sub>2</sub>, HF, HCl, SO<sub>2</sub>, and BrO in the downwind plume of Mt. Etna. *Atmos. Meas. Tech.* 10, 1–14. doi:10.5194/amt-10-1-2017
- Campion, R., Delgado-Granados, H., and Mori, T. (2014). Image-based correction of the light dilution effect for SO<sub>2</sub> camera measurements. *J. Volcanol. Geotherm. Res.* 300, 48–57. doi:10.1016/j.jvolgeores.2015.01.004
- Carboni, E., Grainger, R. G., Mather, T. A., Pyle, D. M., Thomas, G. E., Siddans, R., et al. (2016). The vertical distribution of volcanic SO<sub>2</sub> plumes measured by IASI. *Atmos. Chem. Phys.* 16, 4343–4367. doi:10.5194/acp-16-4343-2016
- Carey, S., and Bursik, M. (2015). “Volcanic plumes,” in *The encyclopedia of volcanoes* (Elsevier), 571–585. doi:10.1016/B978-0-12-385938-9.00032-8
- Carlsen, H. K., Ilyinskaya, E., Baxter, P. J., Schmidt, A., Thorsteinsson, T., Pfeffer, M. A., et al. (2021). Increased respiratory morbidity associated with exposure to a mature volcanic plume from a large Icelandic fissure eruption. *Nat. Commun.* 12, 2161. doi:10.1038/s41467-021-22432-5
- Carn, S. A., Krueger, A. J., Krotkov, N. A., Yang, K., and Evans, K. (2009). Tracking volcanic sulfur dioxide clouds for aviation hazard mitigation. *Nat. Hazards* 51, 325–343. doi:10.1007/s11069-008-9228-4
- Clarisse, L., Hurtmans, D., Clerbaux, C., Hadji-Lazaro, J., Ngadi, Y., and Coheur, P.-F. (2012). Retrieval of sulphur dioxide from the infrared atmospheric sounding interferometer (IASI). *Atmos. Meas. Tech.* 5, 581–594. doi:10.5194/amt-5-581-2012
- Deguine, A., Petitprez, D., Clarisse, L., Gudmundsson, S., Outes, V., Villarosa, G., et al. (2020). Complex refractive index of volcanic ash aerosol in the infrared, visible, and ultraviolet. *Appl. Opt.* 59, 884–895. doi:10.1364/AO.59.000884
- Delmelle, P. (2003). Environmental impacts of tropospheric volcanic gas plumes. *Geol. Soc. Lond. Spec. Publ.* 213, 381–399. doi:10.1144/GSL.SP.2003.213.01.23
- Dudhia, A. (2017). The reference forward model (RFM). *J. Quantitative Spectrosc. Radiat. Transf.* 186, 243–253. doi:10.1016/j.jqsrt.2016.06.018
- Duffell, H., Oppenheimer, C., and Burton, M. (2001). Volcanic gas emission rates measured by solar occultation spectroscopy. *Geophys. Res. Lett.* 28, 3131–3134. doi:10.1029/2000GL012425
- Eatough, D. J., Caka, F. M., and Farber, R. J. (1994). The conversion of SO<sub>2</sub> to sulfate in the atmosphere. *Israel J. Chem.* 34, 301–314. doi:10.1002/ijch.199400034
- Ebmeier, S. K., Sayer, A. M., Grainger, R. G., Mather, T. A., and Carboni, E. (2014). Systematic satellite observations of the impact of aerosols from passive volcanic degassing on local cloud properties. *Atmos. Chem. Phys.* 14, 10601–10618. doi:10.5194/acp-14-10601-2014
- Edmonds, M., and Gerlach, T. M. (2007). Vapor segregation and loss in basaltic melts. *Geology* 35, 751–754. doi:10.1130/G23464A.1
- Esse, B., Burton, M., Varnam, M., Kazahaya, R., and Salerno, G. (2020). iFit: A simple method for measuring volcanic SO<sub>2</sub> without a measured Fraunhofer reference spectrum. *J. Volcanol. Geotherm. Res.* 163, 107000. doi:10.1016/j.jvolgeores.2020.107000
- Francis, P., Burton, M. R., and Oppenheimer, C. (1998). Remote measurements of volcanic gas compositions by solar occultation spectroscopy. *Nature* 396, 567–570. doi:10.1038/25115
- Freret-Lorgeril, V., Donnadiou, F., Eychenne, J., Soriaux, C., and Latchimy, T. (2019). *In situ* terminal settling velocity measurements at Stromboli volcano: Input from physical characterization of ash. *J. Volcanol. Geotherm. Res.* 374, 62–79. doi:10.1016/j.jvolgeores.2019.02.005
- Freret-Lorgeril, V., Gilchrist, J., Donnadiou, F., Jellinek, A. M., Delanoë, J., Latchimy, T., et al. (2020). Ash sedimentation by fingering and sediment thermals from wind-affected volcanic plumes. *Earth Planet. Sci. Lett.* 534, 116072. doi:10.1016/j.epsl.2020.116072
- Goff, F., Love, S. P., Warren, R. G., Counce, D., Obenholzer, J., Siebe, C., et al. (2001). Passive infrared remote sensing evidence for large, intermittent CO<sub>2</sub> emissions at Popocatepetl volcano, Mexico. *Chem. Geol.* 177, 133–156. doi:10.1016/S0009-2541(00)00387-9
- Gudmundsson, G. (2011). Respiratory health effects of volcanic ash with special reference to Iceland. A review: Respiratory health effects of volcanic ash. *Clin. Respir. J.* 5, 2–9. doi:10.1111/j.1752-699X.2010.00231.x
- Guerzanti, H., Sellitto, P., Cuesta, J., Eremenko, M., Lachatre, M., Mailler, S., et al. (2021). Quantitative retrieval of volcanic sulphate aerosols from IASI observations. *Remote Sens.* 13, 1808. doi:10.3390/rs13091808
- Henderson, M. J. B., Horgan, B. H. N., Rowe, M. C., Wall, K. T., and Scudder, N. A. (2021). Determining the volcanic eruption style of tephra deposits from infrared spectroscopy. *Earth Space Sci.* 8. doi:10.1029/2019EA001013
- Horrocks, L., Burton, M., Francis, P., and Oppenheimer, C. (1999). Stable gas plume composition measured by OP-FTIR spectroscopy at Masaya Volcano, Nicaragua, 1998–1999. *Geophys. Res. Lett.* 26, 3497–3500. doi:10.1029/1999GL008383
- Horrocks, L. A., Oppenheimer, C., Burton, M. R., Duffell, H. J., Davies, N. M., Martin, N. A., et al. (2001). Open-path Fourier transform infrared spectroscopy of SO<sub>2</sub>: An empirical error budget analysis, with implications for volcano monitoring. *J. Geophys. Res.* 106, 27647–27659. doi:10.1029/2001JD000343
- Horwell, C. J. (2007). Grain-size analysis of volcanic ash for the rapid assessment of respiratory health hazard. *J. Environ. Monit.* 9, 1107–1115. doi:10.1039/b710583p
- Ilyinskaya, E., Schmidt, A., Mather, T. A., Pope, F. D., Witham, C., Baxter, P., et al. (2017). Understanding the environmental impacts of large fissure eruptions: Aerosol and gas emissions from the 2014–2015 Holuhraun eruption (Iceland). *Earth Planet. Sci. Lett.* 472, 309–322. doi:10.1016/j.epsl.2017.05.025
- Kern, C., Deutschmann, T., Vogel, L., Wöhrbach, M., Wagner, T., and Platt, U. (2010). Radiative transfer corrections for accurate spectroscopic measurements of volcanic gas emissions. *Bull. Volcanol.* 72, 233–247. doi:10.1007/s00445-009-0313-7
- Kern, C., Deutschmann, T., Werner, C., Sutton, A. J., Elias, T., and Kelly, P. J. (2012). Improving the accuracy of SO<sub>2</sub> column densities and emission rates obtained from upward-looking UV-spectroscopic measurements of volcanic plumes by taking realistic radiative transfer into account. *J. Geophys. Res.* Atmos. 117, D20302. doi:10.1029/2012JD017936
- Kern, C., Werner, C., Elias, T., Sutton, A. J., and Lübcke, P. (2013). Applying UV cameras for SO<sub>2</sub> detection to distant or optically thick volcanic plumes. *J. Volcanol. Geotherm. Res.* 262, 80–89. doi:10.1016/j.jvolgeores.2013.06.009
- Kern, C., Aiuppa, A., and de Moor, J. M. (2022). A golden era for volcanic gas geochemistry? *Bull. Volcanol.* 84, 43. doi:10.1007/s00445-022-01556-6
- La Spina, A., Burton, M., and Salerno, G. G. (2010). Unravelling the processes controlling gas emissions from the central and northeast craters of Mt. Etna. *J. Volcanol. Geotherm. Res.* 198, 368–376. doi:10.1016/j.jvolgeores.2010.09.018

- La Spina, A., Burton, M. R., Harig, R., Mure, F., Rusch, P., Jordan, M., et al. (2013). New insights into volcanic processes at Stromboli from Cerberus, a remote-controlled open-path FTIR scanner system. *J. Volcanol. Geotherm. Res.* 249, 66–76. doi:10.1016/j.jvolgeores.2012.09.004
- La Spina, A., Burton, M., Allard, P., Alparone, S., and Muri<sup>1</sup>/<sub>2</sub>, F. (2015). Open-path FTIR spectroscopy of magma degassing processes during eight lava fountains on Mount Etna. *Earth Planet. Sci. Lett.* 413, 123–134. doi:10.1016/j.epsl.2014.12.038
- Love, S. P., Goff, F., Counce, D., Siebe, C., and Delgado-Granados, H. (1998). Passive infrared spectroscopy of the eruption plume at Popocatepetl volcano, Mexico. *Nature* 396, 563–567. doi:10.1038/25109
- Love, S. P., Goff, F., Schmidt, S. C., Counce, D., Pettit, D., Christenson, B. W., et al. (2000). “Passive infrared spectroscopic remote sensing of volcanic gases: Ground-based studies at White Island and Ruapehu, New Zealand, and Popocatepetl, Mexico,” in *Geophysical monograph series*. Editors P. J. Mouginiis-Mark, J. A. Crisp, and J. H. Fink (Washington, D. C.: American Geophysical Union), 117–138. doi:10.1029/GM116p0117
- Lund Myhre, C. E., Christensen, D. H., Nicolaisen, F. M., and Nielsen, C. J. (2003). Spectroscopic study of aqueous H<sub>2</sub>SO<sub>4</sub> at different temperatures and compositions: Variations in dissociation and optical properties. *J. Phys. Chem. A* 107, 1979–1991. doi:10.1021/jp026576n
- Lyon, R. J. P. (1965). Analysis of rocks by spectral infrared emission (8 to 25 microns). *Econ. Geol.* 60, 715–736. doi:10.2113/gsecongeo.60.4.715
- Mather, T. A., Allen, A. G., Oppenheimer, C., Pyle, D. M., and McGonigle, A. J. S. (2003a). Size-Resolved characterisation of soluble ions in the particles in the tropospheric plume of Masaya volcano, Nicaragua: Origins and plume processing. *J. Atmos. Chem.* 46, 207–237. doi:10.1023/a:1026327502060
- Mather, T. A., Pyle, D. M., and Oppenheimer, C. (2003b). “Tropospheric volcanic aerosol,” in *Geophysical monograph series*. Editors A. Robock and C. Oppenheimer (Washington, D. C.: American Geophysical Union), 189–212. doi:10.1029/139GM12
- Mather, T. A., Oppenheimer, C., Allen, A. G., and McGonigle, A. J. S. (2004a). Aerosol chemistry of emissions from three contrasting volcanoes in Italy. *Atmos. Environ.* 38, 5637–5649. doi:10.1016/j.atmosenv.2004.06.017
- Mather, T. A., Tsanev, V. I., Pyle, D. M., McGonigle, A. J. S., Oppenheimer, C., and Allen, A. G. (2004b). Characterization and evolution of tropospheric plumes from Lascar and Villarrica volcanoes, Chile. *J. Geophys. Research-Atmospheres* 109. doi:10.1029/2004JD004934
- Mather, T. A. (2015). Volcanoes and the environment: Lessons for understanding Earth’s past and future from studies of present-day volcanic emissions. *J. Volcanol. Geotherm. Res.* 304, 160–179. doi:10.1016/j.jvolgeores.2015.08.016
- McGonigle, A. J. S., Delmelle, P., Oppenheimer, C., Tsanev, V. I., Delfosse, T., Williams-Jones, G., et al. (2004). SO<sub>2</sub> depletion in tropospheric volcanic plumes: Volcanic SO<sub>2</sub> depletion. *Geophys. Res. Lett.* 31. doi:10.1029/2004GL019990
- Michalski, J. R. (2004). Thermal infrared analysis of weathered granitic rock compositions in the Sacaton Mountains, Arizona: Implications for petrologic classifications from thermal infrared remote-sensing data. *J. Geophys. Res.* 109, E03007–E03015. doi:10.1029/2003JE002197
- Mori, T., and Notsu, K. (1997). Remote CO, COS, CO<sub>2</sub>, SO<sub>2</sub>, HCl detection and temperature estimation of volcanic gas. *Geophys. Res. Lett.* 24, 2047–2050. doi:10.1029/97GL52058
- Mori, T., Notsu, K., Tohjima, Y., Wakita, H., Nuccio, P. M., and Italiano, F. (1995). Remote detection of fumarolic gas chemistry at Vulcano, Italy, using an FT-IR spectral radiometer. *Earth Planet. Sci. Lett.* 134, 219–224. doi:10.1016/0012-821X(95)00119-W
- Notsu, K., Mori, T., Igarashi, G., Tohjima, Y., and Wakita, H. (1993). Infrared spectral radiometer: A new tool for remote measurement of SO<sub>2</sub> of volcanic gas. *Geochem. J.* 27, 361–366. doi:10.2343/geochemj.27.361
- Oppenheimer, C., Francis, P., Burton, M., Maciejewski, A. J. H., and Boardman, L. (1998a). Remote measurement of volcanic gases by Fourier transform infrared spectroscopy. *Appl. Phys. B Lasers Opt.* 67, 505–515. doi:10.1007/s003400050536
- Oppenheimer, C., Francis, P., and Stix, J. (1998b). Depletion rates of sulfur dioxide in tropospheric volcanic plumes. *Geophys. Res. Lett.* 25, 2671–2674. doi:10.1029/98GL01988
- Patrick, M. R., Harris, A. J. L., Ripepe, M., Dehn, J., Rothery, D. A., and Calvari, S. (2007). Strombolian explosive styles and source conditions: Insights from thermal (FLIR) video. *Bull. Volcanol.* 69, 769–784. doi:10.1007/s00445-006-0107-0
- Pfeffer, M., Bergsson, B., Barsotti, S., Stefánsdóttir, G., Galle, B., Arellano, S., et al. (2018). Ground-based measurements of the 2014–2015 holuhraun volcanic cloud (Iceland). *Geosciences* 8, 29. doi:10.3390/geosciences8010029
- Pianezze, J., Tulet, P., Foucart, B., Leriche, M., Liuzzo, M., Salerno, G., et al. (2019). Volcanic plume aging during passive degassing and low eruptive events of Etna and Stromboli volcanoes. *J. Geophys. Res. Atmos.* 124, 11389–11405. doi:10.1029/2019JD031122
- Piontek, D., Hornby, A. J., Voigt, C., Bugliaro, L., and Gasteiger, J. (2021). Determination of complex refractive indices and optical properties of volcanic ashes in the thermal infrared based on generic petrological compositions. *J. Volcanol. Geotherm. Res.* 411, 107174. doi:10.1016/j.jvolgeores.2021.107174
- Prata, G. S., Ventress, L. J., Carboni, E., Mather, T. A., Grainger, R. G., and Pyle, D. M. (2019). A new parameterization of volcanic ash complex refractive index based on NBO/T and SiO<sub>2</sub> content. *J. Geophys. Res. Atmos.* 124, 1779–1797. doi:10.1029/2018JD028679
- Ramsey, M. S., and Christensen, P. R. (1998). Mineral abundance determination Quantitative deconvolution of thermal emission spectra. *J. Geophys. Res.* 103, 577–596. doi:10.1029/97JB02784
- Reed, B. E., Peters, D. M., McPheat, R., and Grainger, R. G. (2018). The complex refractive index of volcanic ash aerosol retrieved from spectral mass extinction. *J. Geophys. Res. Atmos.* 123, 1339–1350. doi:10.1002/2017JD027362
- Roberts, T. J., Vignelles, D., Liuzzo, M., Giudice, G., Aiuppa, A., Coltelli, M., et al. (2018). The primary volcanic aerosol emission from Mt Etna: Size-resolved particles with SO<sub>2</sub> and role in plume reactive halogen chemistry. *Geochimica Cosmochimica Acta* 222, 74–93. doi:10.1016/j.gca.2017.09.040
- Rodríguez, L. A., Watson, I. M., Edmonds, M., Ryan, G., Hards, V., Oppenheimer, C. M. M., et al. (2008). SO<sub>2</sub> loss rates in the plume emitted by Soufrière Hills volcano, Montserrat. *J. Volcanol. Geotherm. Res.* 173, 135–147. doi:10.1016/j.jvolgeores.2008.01.003
- Rogers, A. D., and Nekvasil, H. (2015). Feldspathic rocks on mars: Compositional constraints from infrared spectroscopy and possible formation mechanisms: Feldspathic rocks on mars: Constraints. *Geophys. Res. Lett.* 42, 2619–2626. doi:10.1002/2015GL063501
- Rothman, L. S., Gordon, I. E., Barbe, A., Benner, D. C., Bernath, P. F., Birk, M., et al. (2009). The HITRAN 2008 molecular spectroscopic database. *J. Quantitative Spectrosc. Radiat. Transf.* 110, 533–572. doi:10.1016/j.jqsrt.2009.02.013
- Rufus, J., Stark, G., Smith, P. L., Pickering, J. C., and Thorne, A. P. (2003). High-resolution photoabsorption cross section measurements of SO<sub>2</sub>, 2: 220 to 325 nm at 295 K: SO<sub>2</sub> photoabsorption cross sections. *J. Geophys. Res.* 108. doi:10.1029/2002JE001931
- Sahyoun, M., Freney, E., Brito, J., Duplissy, J., Gouhier, M., Colomb, A., et al. (2019). Evidence of new particle formation within Etna and Stromboli volcanic plumes and its parameterization from airborne *in situ* measurements. *J. Geophys. Res. Atmos.* 124, 5650–5668. doi:10.1029/2018JD028882
- Schmidt, A., Witham, C. S., Theys, N., Richards, N. A. D., Thordarson, T., Szpek, K., et al. (2014). Assessing hazards to aviation from sulfur dioxide emitted by explosive Icelandic eruptions. *J. Geophys. Res. Atmos.* 119, 14180–14196. doi:10.1002/2014JD022070
- Sellitto, P., Guermazi, H., Carboni, E., Siddans, R., and Burton, M. (2019). Unified observation co-existing volcanic sulphur dioxide and sulphate aerosols using ground-based Fourier transform infrared spectroscopy. *Atmos. Meas. Tech. Discuss.*, 1–12. doi:10.5194/amt-2019-186
- Sellitto, P., Salerno, G., Spina, A. L., Caltabiano, T., Boselli, A., Leto, G., et al. (2020). Small-scale volcanic aerosols variability, processes and direct radiative impact at Mount Etna during the EPL-RADIO campaigns. *Sci. Rep.* 1, 15224–15313. doi:10.1038/s41598-020-71635-1
- Sellitto, P., Salerno, G., Doussin, J.-F., Triquet, S., Dulac, F., and Desboeufs, K. (2021). Photometric observations of aerosol optical properties and emission flux rates of Stromboli volcano plume during the PEACETIME campaign. *Remote Sens.* 13, 4016. doi:10.3390/rs13194016
- Sellitto, P., and Legras, B. (2016). Sensitivity of thermal infrared nadir instruments to the chemical and microphysical properties of UTLS secondary sulfate aerosols. *Atmos. Meas. Tech.* 9, 115–132. doi:10.5194/amt-9-115-2016
- Serduchenko, A., Gorshelev, V., Weber, M., Chehade, W., and Burrows, J. P. (2014). High spectral resolution ozone absorption cross-sections – Part 2: Temperature dependence. *Atmos. Meas. Tech.* 7, 625–636. doi:10.5194/amt-7-625-2014
- Siegel, A. F. (1982). Robust regression using repeated medians. *Biometrika* 69, 242–244. doi:10.1093/biomet/69.1.242
- Sigmundsson, F., Hreinsdóttir, S., Hooper, A., Árnadóttir, T., Pedersen, R., Roberts, M. J., et al. (2010). Intrusion triggering of the 2010 Eyjafjallajökull explosive eruption. *Nature* 468, 426–430. doi:10.1038/nature09558
- Stremme, W., Krueger, A., Harig, R., and Grutter, M. (2012). Volcanic SO<sub>2</sub> and SiF<sub>4</sub> visualization using 2-D thermal emission spectroscopy Part 1: Slant-columns and their ratios. *Atmos. Meas. Tech.* 5, 275–288. doi:10.5194/amt-5-275-2012
- Sumlin, B. J., Heinson, W. R., and Chakrabarty, R. K. (2018). Retrieving the aerosol complex refractive index using PyMieScatt: A Mie computational package

with visualization capabilities. *J. Quantitative Spectrosc. Radiat. Transf.* 205, 127–134. doi:10.1016/j.jqsrt.2017.10.012

Tang, Y., Tong, D. Q., Yang, K., Lee, P., Baker, B., Crawford, A., et al. (2020). Air quality impacts of the 2018 Mt. Kilauea volcano eruption in Hawaii: A regional chemical transport model study with satellite-constrained emissions. *Atmos. Environ.* 237, 117648. doi:10.1016/j.atmosenv.2020.117648

Taquet, N., Meza Hernández, L., Stremme, W., Bezanilla, A., Grutter, M., Campion, R., et al. (2017). Continuous measurements of SiF<sub>4</sub> and SO<sub>2</sub> by thermal emission spectroscopy: Insight from a 6-month survey at the Popocatepetl volcano. *J. Volcanol. Geotherm. Res.* 341, 255–268. doi:10.1016/j.jvolgeores.2017.05.009

Taquet, N., Stremme, W., Grutter, M., Baylón, J., Bezanilla, A., Schiavo, B., et al. (2019). Variability in the gas composition of the popocatepetl volcanic plume. *Front. Earth Sci.* 7, 1–14. doi:10.3389/feart.2019.00114

Vanderkluyzen, L. L., Burton, M. R., Clarke, A. B., Hartnett, H. E., and Smekens, J. F. F. (2014). Composition and flux of explosive gas release at LUSI mud volcano (East Java, Indonesia). *Geochem. Geophys. Geosystems* 15, 2932–2946. doi:10.1002/2014GC005275

Varnam, M., Burton, M., Esse, B., Kazahaya, R., Salerno, G., Caltabiano, T., et al. (2020). Quantifying light dilution in ultraviolet spectroscopic measurements of volcanic SO<sub>2</sub> using dual-band modeling. *Front. Earth Sci.* 8, 1–11. doi:10.3389/feart.2020.528753

Whitby, K. T. (1978). “The physical characteristics of sulfur aerosols,” in *Sulfur in the atmosphere* (Elsevier), 135–159. doi:10.1016/B978-0-08-022932-4.50018-5

Wilson, G., Wilson, T. M., Deligne, N. I., and Cole, J. W. (2014). Volcanic hazard impacts to critical infrastructure: A review. *J. Volcanol. Geotherm. Res.* 286, 148–182. doi:10.1016/j.jvolgeores.2014.08.030